DYNAMIC-ACTIVE FLOW CONTROL - PHASE I

By

ASHLEY TUCK AND JULIO SORIA[1]

Laboratory for Turbulence Research in Aerospace and
Combustion
Department of Mechanical Engineering
Monash University
Melbourne Australia

AOARD Project ID: FA5209-05-T-0435

[1] Address correspondence to: Professor Julio Soria, LTRAC, Department of Mechanical Engineering, Monash University, Melbourne, VIC 3800, Australia.
Email: Julio.soria@eng.monash.edu.au

Report Documentation Page

1. REPORT DATE **18 OCT 2006**	2. REPORT TYPE **Final Report (Technical)**	3. DATES COVERED **01-06-2005 to 01-08-2006**

4. TITLE AND SUBTITLE **Dynamic-Active Flow Control**	5a. CONTRACT NUMBER
	5b. GRANT NUMBER
	5c. PROGRAM ELEMENT NUMBER
6. AUTHOR(S) **Julio Soria**	5d. PROJECT NUMBER
	5e. TASK NUMBER
	5f. WORK UNIT NUMBER

7. PERFORMING ORGANIZATION NAME(S) AND ADDRESS(ES) **Monash University,Wellington Road,Clayton VIC 3129,Australia,AU,3129**	8. PERFORMING ORGANIZATION REPORT NUMBER **AOARD-054039**

9. SPONSORING/MONITORING AGENCY NAME(S) AND ADDRESS(ES) **The US Resarch Labolatory, AOARD/AFOSR, Unit 45002, APO, AP, 96337-5002**	10. SPONSOR/MONITOR'S ACRONYM(S) **AOARD/AFOSR**
	11. SPONSOR/MONITOR'S REPORT NUMBER(S)

12. DISTRIBUTION/AVAILABILITY STATEMENT
Approved for public release; distribution unlimited

13. SUPPLEMENTARY NOTES

14. ABSTRACT

This is the report of an investigation of active flow control using a wall-normal, zero-net-mass-flux (ZNMF) jet located at the leading edge of an airfoil.

15. SUBJECT TERMS
Flow Control, Active Control

16. SECURITY CLASSIFICATION OF:			17. LIMITATION OF ABSTRACT	18. NUMBER OF PAGES	19a. NAME OF RESPONSIBLE PERSON
a. REPORT **unclassified**	b. ABSTRACT **unclassified**	c. THIS PAGE **unclassified**		**60**	

CONTENTS

NOMENCLATURE

A	Amplitude of piston displacement
A_j	Jet exit area
A_p	Piston area
c	Airfoil chord length
c_D	Drag coefficient
c_L	Lift coefficient
c_{L0}	Uncontrolled lift coefficient
c_μ	Oscillatory momentum blowing coefficient: $c_\mu \equiv 2\dfrac{h}{c}\left(\dfrac{u_{j\,rms}}{U_\infty}\right)^2$
f	Excitation frequency
F^+	Non-dimensional frequency: $\qquad F^+ \equiv \dfrac{fc}{U_\infty}$
h	Slot height
IW	Interrogation window dimension
L	Slot length
M	PIV magnification factor
$P_{control}$	Power consumed by the actuator
P_{cruise}	Aircraft drag power under cruising conditions
PLIF	Planar laser induced fluorescence
ρ	Density of working fluid
Re	Reynolds number: $\qquad \mathrm{Re} \equiv \dfrac{U_\infty c}{\nu}$
S	Planform area of airfoil
St	Strouhal number
Δt	Time delay between PIV images
$t_{control}$	Duration that control is applied
t_{cruise}	Aircraft cruising time
u	x-component of velocity
$u_{j\,rms}$	RMS jet velocity in the exit plane
$u_{j\,max}$	Peak jet velocity in the exit plane
$u_{p\,rms}$	RMS piston velocity
U_∞	Freestream velocity
v	y-component of velocity
VR	Velocity ratio: $\qquad VR \equiv \dfrac{u_{j\,rms}}{U_\infty}$
ω	Rotational speed of stepper motor
ω_z	Out of plane vorticity
ω'_z	Non-dimensionalised vorticity: $\qquad \omega'_z \equiv \dfrac{\omega_z c}{U_\infty}$
x	Chordwise airfoil coordinate
ZNMF	Zero-net-mass-flux

SUMMARY

The effect of using a wall-normal, zero-net-mass-flux (ZNMF) jet located at the leading edge of a NACA 0015 airfoil as an active flow control device has been investigated. The study employed a two-dimensional airfoil fitted with a leading edge slot that extended over the entire span of the airfoil. Parametric investigations were conducted in a water tunnel at a Reynolds number of 3.08×10^4. The optimal forcing frequencies were found to be symmetrically offset from a non-dimensional forcing frequency of unity, at $F^+ = 0.7$ and 1.3. At these optimal forcing frequencies the lift coefficient increase above the uncontrolled case for post-stall angles of attack was found to be approximately proportional to the square root of the jet momentum, which can otherwise be interpreted as being linearly proportional to the jet velocity ratio. Under the optimal forcing conditions the stall angle of the airfoil was delayed from an angle of attack of 10° to an angle of attack of 18°, resulting in a maximum lift coefficient increase of 46% above the uncontrolled lift coefficient. Significant improvement in the lift to drag ratio of the airfoil was also noted throughout the post-stall region investigated.

Dye streak flow visualisations revealed that at an angle of attack of 18° a massive wake region was present over the upper surface of the uncontrolled airfoil. Activation of the control resulted in what appeared to be full reattachment of the flow to the upper airfoil surface.

Planar laser induced fluoroscopy (PLIF) was conducted by introducing a small amount of fluorescent dye into the ZNMF jet cavity at a reduced Reynolds number of 1.54×10^4. Illumination of this dye in the mid-plane of the airfoil using a laser sheet, shed some light on the structure of the controlled flow field. The reattachment of the flow was attributed to the generation of a train of large-scale, spanwise lifting vortices that appear to roll down the upper surface of the airfoil. These results suggest that the structures responsible for reattachment of the flow are all negatively rotating vortices, which are larger than two orders of magnitude larger compared to the characteristic dimension of the ZNMF jet orifice.

The optimum forcing frequencies were observed to correspond to vortex residence durations over the suction surface of one and two excitation periods for the lower and higher optimal frequencies respectively. The negatively rotating vortex generated by the ZNMF jet was seen to be amplified by the natural shear layer, whist the positively rotating vortex was destructively interfered with by the same shear layer, such that its presence was not observed at any time over the suction surface.

The reattachment of the flow at high angles of attack by the train of spanwise vortices was postulated to occur through three primary mechanisms: enhanced entrainment of the shear layer by the addition of large-scale vorticity, deflection of the shear layer by the transfer of rotational momentum from the negatively rotating vortex, and the alleviation of the adverse pressure gradient upstream of the vortex due to the deflection of streamlines around the vortex that resided over the upper surface of the airfoil.

1.0 INTRODUCTION

Flow control over airfoils is primarily directed at increasing the lift and decreasing the drag produced by an airfoil. This is most often achieved by manipulating the boundary and shear layer flows, in order to minimise the separation region on the suction surface of the airfoil. Flow control techniques can be classified into two distinct regimes, active and passive control.

Active flow control refers to the process of expending energy in order to modify the flow (Donovan, Kral and Cary, 1998). This is distinct from passive techniques where flow control is provided without expending energy through means such as geometric shaping. One of the main advantages of active, rather than passive, flow control is that the control device can be switched off when it is not required. This avoids unnecessary drag penalties that are inherent in passive control techniques when the control is not being utilized. For example, the stability of the boundary layer on the upper surface of a wing can be increased at high angles of attack through the use of a leading edge strake or some other form of vortex generator. However, these systems will impose a drag penalty at lower angles of attack when the control system is not required. Active control methods could be employed to achieve a similar result at high angles of attack, and could be switched off at lower angles, imposing no unnecessary impediment to the flow.

The first application of active flow control was the use of steady suction through a slot to remove the low energy fluid from the boundary layer close to the wall, as postulated by Prandtl in 1904 (Houghton and Carpenter, 2003). The resulting boundary layer is thinner with a 'healthier' velocity profile that is less susceptible to separation. Tangential boundary layer blowing works by a similar manner, however rather than removing the low energy fluid, this fluid is re-energized by the injection of high-speed fluid in the near wall region. The concept of boundary layer blowing can be extended even further by making use of the Coanda effect. The Coanda effect is the phenomenon whereby a flow tends to adhere to the contour of a continuous surface (McCormick, 1995, p.446). Making use of this phenomenon a wall jet can be used to assist the boundary layer to remain attached to the surface. More recently, techniques whereby the primary active control mechanism is the addition of vorticity to the flow field have been proposed. These techniques include piezoelectric devices, vibrating flaperons, oscillating wires and the zero-net-mass-flux (ZNMF) jet that has been studied in this investigation.

A ZNMF jet, also known as a synthetic jet, 'transfers linear momentum to the flow system without net mass injection across the system boundary' (Smith and Glezer, 1998). ZNMF jets are commonly formed using a sinusoidally oscillating membrane to alternatively force fluid through an orifice into the flow field and then to entrain fluid back through the orifice. During the forcing stroke the ejected fluid separates at the sharp edges of the orifice, forming a shear layer. This layer of vorticity rolls up to form a vortex ring for the case of a round synthetic jet or a vortex pair for the case of a plane synthetic jet (Lee, Hong and Mallinson, 2003). The vortex pair (or ring) moves away from the orifice under its own momentum. By the time the membrane begins its intake stroke, the vortex pair is 'sufficiently distant from the orifice that it is virtually unaffected by the entrainment of fluid into the cavity' (Lee, Hong and Mallinson, 2003). For every oscillation period of the membrane a single vortex pair is formed. However, as the motion of the membrane is periodic, a constant train of vortices that convect away from the ZNMF jet orifice is created. At some distance from the jet orifice, the

discrete vortex pairs slow down, lose their coherence and ultimately undergo a transition to turbulence. This transition is followed by the emergence of a fully developed turbulent jet (Smith and Glezer, 1998).

The velocity distribution of a ZNMF jet has been found to be similar to that of a continuous jet, however greater spreading rates and larger decay constants have been noted for the ZNMF jet (Cater and Soria, 2002). The greater spreading rates and more rapid decay of centerline velocity in the ZNMF jet can be attributed to greater radial entrainment, due primarily to the augmented presence of large-scale structures in the jet shear layers. Due to the more rapid decay of the centerline velocity, the ZNMF jet does not penetrate as deeply into the global flow field as a comparable continuous jet. It is postulated that for active flow control techniques requiring the addition of large-scale vorticity, the use of ZNMF jets is likely to be more efficient than the use of equivalent continuous jets for the aforementioned reasons. ZNMF jets offer many other advantages in terms of simplicity over continuous jets. These advantages stem primarily from the fact that the ZNMF jet requires no time-averaged net mass transfer through the orifice. Hence, no sources of additional fluid, or ducting required to channel this fluid are required. ZNMF jets can be manufactured at micron scales using micro-piezoelectric manufacturing technology (Cater and Soria, 2002, p.168). This allows for the possibility of implementing ZNMF jets at smaller length scales than would be possible with equivalent continuous jets.
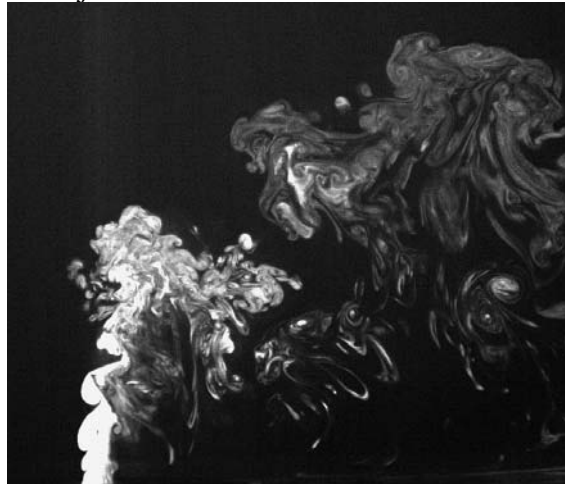

Figure 1.1 - ZNMF Jet in Cross-flow. Image courtesy of S. Tomar, Laboratory for Turbulence Research in Aerospace and Combustion, Monash University, Australia.

ZNMF jets may be oriented at any angle with respect to the local freestream velocity in active flow control applications. This investigation considers only the case where the principle axis of the ZNMF jet is normal to the boundary surface. In this case a ZNMF jet in cross-flow scenario is effectively created. Tomar, Arnaud and Soria (2004) have studied the characteristics of circular ZNMF jets in cross-flow for a range of different velocity ratios and forcing frequencies. A typical flow visualisation for a ZNMF jet in cross flow is depicted in figure 1.1. Clearly evident from the figure is the complex vortical structures generated by the interaction of the ZNMF jet with the cross-stream flow. Tomar, Arnaud and Soria (2004) have determined that at low Strouhal numbers ($St < 0.113$) the ZNMF jet, with its incorporated vorticity, is aligned along a single principal trajectory. At Strouhal numbers greater than 0.188 the ZNMF jet in cross-flow is characterised by two dominant trajectories. It is quite plausible that this critical Strouhal number, which characterises the ZNMF jet's structure, will play an

important role in determining the effectiveness of the ZNMF jet as an active flow control device.

Active flow control is a highly multi-disciplinary research area. Due to the inherent interaction of two or more fluid streams, turbulent flow physics is a prevailing topic. The complicated constructive and destructive interaction of different flow frequencies, for example the forcing frequencies, boundary layer instability frequencies and turbulent shear layer shedding frequencies, adds further complication to the discipline. The areas of sensing and control systems are also invaluable if a complete flow control system is to be implemented. The mechanics of resonating membranes needs also to be quantified if ZNMF jets are to find practical usage. Finally, with periodic forcing systems such as ZNMF jets, the interaction between the excitation frequencies and any structural vibration modes requires quantification.

A wide range of potential applications exists for active flow control. It could be used to mitigate stall effects and hence act as a lift enhancement device in place of mechanically complicated flaps and slats. In this regard ZNMF jets could possibly offer weight savings due to the simplicity of the device. As ZNMF control devices can be activated without the deflection of any surfaces they may find some application in military circumstances where retaining a minimum radar cross-section is critical. In emergency situations a ZNMF jet may be able to be activated quicker than a flap could be deployed. This makes a ZNMF jet, coupled with an appropriate control system, an attractive option as a dynamic stall recovery device. Another approach that could be explored is to use the greater adverse pressure gradients that can be overcome by an actively controlled airfoil to design thicker, more structurally efficient airfoils. In this case the control device would indirectly affect a drag saving on the aircraft through a minimization of induced drag.

2.0 PROJECT AIMS

This project aimed to investigate the effect of using a ZNMF jet located at the leading edge of a NACA 0015 airfoil as an active flow control device. The 2-dimensional jet employed was normal to the local boundary surface with an average slot height of 0.155% of the chord length. The study was limited to the investigation of an ideally 2-dimensional flow field at Reynolds numbers of between 1.5×10^4 and 4×10^4.

The effect imparted on the airfoil by the ZNMF jet was quantified by measuring the lift and drag forces acting on the airfoil. Using the force measurements the forcing parameters leading to the largest lift enhancements were identified. The flow field around the airfoil under the optimal forcing conditions was characterised using flow visualisations, planar laser induced florescence (PLIF).

3.0 LITERATURE REVIEW

The first use of velocity perturbations to actively control a flow field under similar circumstances to those that will be examined in this investigation was in the form of transverse velocity waves. These velocity waves were introduced into the wind tunnel flow fields through the use of a speaker attached to the tunnel wall. Zaman, Bar-Sever and Mangalam (1987) found that low frequency, low-amplitude excitation in the range of $St \geq 5$ was effective in prohibiting laminar separation bubbles from forming on the suction surface of an airfoil. Excitation at a high frequency eliminated the periodic shedding of large-scale vortices. Higher amplitude excitation was found to increase the lift produced by the airfoil in the post-stall region. They noted that the excitation was most effective at frequencies that resulted in large transverse velocity fluctuations, rather than large amplitude pressure fluctuations.

Zaman (1992) conducted further research in the post-stall region of the airfoil and found that, contrary to his initial postulation, the optimum forcing frequency did not occur at the Kelvin-Helmholtz instability frequency for the separated shear layer. Rather, the effective frequencies were approximately an order of magnitude lower. Thus, he was able to conclude that the primary mechanism through which the control worked was not excitation of the linear instability of the separated shear layer. He also noted that the optimum frequency of excitation decreased as the amplitude of the excitation was increased.

The effect of introducing velocity perturbations into the flow field through the use of an oscillating wire positioned slightly upstream of an airfoil's leading edge was examined by Bar-Sever (1988). Lift increments were only found when the length scale of the vortical structures induced by the oscillating wire was less than the chord length of the airfoil. At frequencies corresponding to this condition it was shown that the periodic forcing effectively reduced the reattachment length of the separated region.

Flow reattachment of an otherwise separated flow field was also achieved using a small vibrating flaperon located at the apex of a divergence in a wind tunnel wall (Katz, Nishiri and Wygnanski, 1989). The frequency of the excitation was noted to have a large impact on the effectiveness of reattachment.

Chang, Hsiao and Shyu (1992) were able to delay the stall angle of a NACA 63_3-018 airfoil from 15° to 22° using acoustic excitation emanating from a slot located 1.25% of the chord length downstream from the leading edge. For angles of attack of 20-22°, when the uncontrolled airfoil had stalled, a threshold frequency, below which excitation was of little benefit was found to exist for a particular forcing level. This threshold frequency was found to be in the order of $St = 2$. At higher forcing levels this threshold was not evident, however with further increase of the forcing level a gradually diminishing effect was noted. Maximum lift increments were found at an angle of attack of 22° where the lift coefficient was increased from 0.6 to 1.1.

Seifert, Bachar, Koss, Shepshelovich and Wygnanski (1993) reported enhanced lift being obtained from a flapped NACA 0015 airfoil, where a combination of steady and oscillatory blowing was applied tangential to the surface from a slot located at the flap hinge. They found that similar increments in lift could be obtained using an order of magnitude less power for the excitation device if an oscillatory component was superimposed on a steady jet, rather than the use of purely a steady jet. Momentum blowing coefficients in the range of 0-0.016 were used in the experiment, while non-dimensional frequencies in the range of 1-3 were found to produce the best results. Results were found to be largely independent of Reynolds number, which the authors

suggest indicates that the enhanced lift cannot be simply a result of the excitation tripping the boundary layer, as this mechanism would produce results highly dependent on Reynolds number.

Using a number of different airfoils and excitation locations, the effect of oscillations superimposed on a steady jet was further investigated by Seifert, Darabi and Wygnanski (1996). It was found that the most effective location for the excitation was that nearest the separation location. For optimal lift increments, it was determined that no more than 2 eddies should exist on the suction surface of the airfoil at any point in time. No oscillation in the lift force produced by the excited airfoil was found when 2 eddies existed over the suction surface of the airfoil. Examination of surface pressures on the airfoil revealed that the effective wavelength of the eddies doubled during their travel from the separation location to the trailing edge. An optimum momentum blowing coefficient was found to exist at $c_\mu \approx 0.05\%$ for oscillatory blowing emanating from the leading edge, whilst a broad maximum in the lift increment was observed centered around $F^+ \approx 0.75$.

The effect of using ZNMF jets operating at higher frequencies (in the order of $2 < F^+ < 20$) was investigated by Smith, Amitay, Kibens, Parekh and Glezer (1998) using a 24% thick airfoil. At these high frequencies they were able to reattach the flow for angles of attack up to 18°. Their analysis postulates that 'interaction between the synthetic jet and the main flow induces a local 'transpirating' recirculation bubble, not dissimilar to natural laminar separation bubbles, which acts as a 'virtual surface' and displaces local streamlines well outside the undisturbed boundary layer.' Results suggest a definite threshold jet momentum, below which the excitation has little effect on the flow field. This threshold magnitude decreases as the excitation location approaches the location of the separation point.

Donovan, Kral and Cary (1998) conducted a numerical simulation of a NACA 0015 airfoil equipped with a tangential oscillatory jet located at the leading edge. Simulations were conducted at a chord Reynolds number of 1.2 x 10^6 using the Spalart-Allmaras turbulence model. The frequency of oscillations used was chosen to be equivalent to the natural shedding frequency for the uncontrolled airfoil, determined to be $F^+ = 0.58$ for $\alpha = 22^o$. Momentum blowing coefficients in the range of 0.02-0.08% were used and found to result in lift coefficient increments in the order of 0.2-0.3 at $\alpha = 22^o$. Velocity vector plots showed that the effect of the actuator was to increase the 'average' attachment of the flow over the suction surface; however regions of separated flow still existed. Instantaneous phase locked velocity vectors depicted large spanwise vortical structures convecting downstream from the actuator location. These structures were claimed to be responsible for the enhanced 'average' attachment of the flow. The large size of these structures when compared to the momentum of the synthetic jet indicated that 'the synthetic jet was modulating the separation point and leading to a change in the global flow field.' The authors do note however that their choice of turbulence model had a significant effect on the results in the large separated regions of the flow field.

Further numerical investigations were conducted by Wu, Lu, Denny, Fan and Wu (1998) using the Reynolds averaged compressible Navier-Stokes equations. The Baldwin-Lomax algebraic turbulence model coupled with the Launder-Sharma wall damping function was employed. Flow control over a NACA 0012 airfoil was implemented using simulated periodic suction-blowing over a slot of height equivalent to 2.5%c. The mesh density used in this investigation was not sufficient for the detail of the jet actuator to be captured. In a distinct contrast to the reduced frequency used by

other researchers the forcing frequency in this study was normalised by the shedding frequency for the uncontrolled airfoil. The most effective forcing frequencies were found to be 1 or 2 times greater than the uncontrolled airfoil shedding frequency, although it was noted that the optimum increase in lift coefficient, decrease in drag coefficient, and improvement of the lift-to-drag ratio all occurred at different forcing frequencies. The authors postulate that below a velocity ratio (defined as the maximum jet exit velocity normalised by the freestream velocity) of 0.1 the excitation does not possess sufficient power to organize, and hence control the flow field. A spectrum of the pressure coefficient from the computational results depicts the presence of a number of peaks located at harmonics of the excitation frequency. The increased lift noted when the excitation was activated was attributed to the forced rolling-up coalescence of the leading edge shear layer vortices. This coalescence was noted to result in stronger shear layer entrainment. In the far field, it was noted that the wake vortices form a row of 'short spaced vortex couples' for the controlled case whereas in the uncontrolled case the wake vortices form a Von-Karámán vortex sheet. This vortex behavior was observed to be associated with a stronger downwash velocity.

In an attempt to isolate the effects of oscillatory control on a fully turbulent boundary layer from the control's effect on a transitional boundary layer, Seifert and Pack (2002) mounted a hump on a wind tunnel wall that had a shape similar to the suction surface of an airfoil. With a fully turbulent boundary layer it was found that Reynolds number only had a weak effect on the flow field in the range of Reynolds numbers tested $(2.4\text{-}26 \times 10^6)$. The superposition of weak steady suction onto the excitation oscillations was observed to 'enhance the receptivity of the separated shear layer.' The authors state an assumption that the upper limit of effective excitation frequencies was the Kelvin-Helmholtz instability of the shear layer, whilst the lower limit of effective frequencies was the natural shedding frequency of the uncontrolled airfoil.

Lee, Hong and Mallinson (2003) investigated the effects of a piezoelectrically driven synthetic jet on an adverse pressure gradient flow. Mean boundary layer velocity profiles were measured using a hot wire. Little difference was found in the velocity profiles when the amplitude of the oscillations was altered, whereas a significant difference was noted with changes in excitation frequency. Results presented suggest a critical forcing amplitude, below which negligible effects were noted in the velocity profile.

The literature presented depicts a number of consistent findings. Firstly, it is widely reported that oscillatory control has positive benefits on both the lift and drag forces generated by an airfoil, particularly in the post-stall region. It is also demonstrated in a number of sources that the effects of ZNMF jet control show little dependence on Reynolds number, except in the case where laminar-turbulent transition effects are significant. Studies where the control actuators have been placed closest to the separation point have reported the most beneficial results. A form of threshold forcing amplitude, below which oscillatory control has only minimal effect, has been reported in a few references. The magnitude of the effective momentum blowing coefficients has been varied, due primarily to differences in location and application of the control. Optimal results have generally been reported for non-dimensional frequencies in the range of 0.58-2. However, other researchers have had success operating at non-dimensional frequencies an order of magnitude higher.

4.0 FLOW PARAMETERISATION

Three primary non-dimensional coefficients can be used to characterise a periodically excited airfoil flow. These parameters are the Reynolds number, the non-dimensional frequency and the oscillatory momentum blowing coefficient.

The Reynolds number is defined in an identical fashion to the Reynolds number for a similar, uncontrolled airfoil based on the chord length, namely:

$$\text{Re} \equiv \frac{U_\infty c}{\nu} \qquad (1)$$

Where U_∞ is the freestream velocity, c is the chord length of the airfoil and ν is the kinematic viscosity of the working fluid.

The second parameter of significance is the non-dimensional frequency. The classic definition for a reduced frequency, comparable to the Strouhal number, is used in this investigation:

$$F^+ \equiv \frac{fc}{U_\infty} \qquad (2)$$

Where f is the excitation frequency. Seifert et al (1996) have proposed an alternative formulation for the non-dimensional frequency. They suggest that the most appropriate length scale to be used in the reduced frequency is the streamwise length of the separated region, x_{sep}, such that:

$$F^+ \equiv \frac{fx_{sep}}{U_\infty} \qquad (3)$$

For most airfoils, such as the one considered in this investigation, once the stall angle is reached the flow separates from a location close to the leading edge, ie: $x_{sep} \approx c$. Therefore, for the geometries being considered in this study the two definitions put forth in equations (2) and (3) are almost identical. For reasons of simplicity the definition proposed in equation (2) is retained.

The momentum of the ZNMF jet is quantified in terms of the oscillatory momentum blowing coefficient. This non-dimensional group is a measure of the momentum flux through the ZNMF jet orifice normalised by a characteristic momentum for the global flow field:

$$c_\mu \equiv 2\frac{h}{c}\left(\frac{u_{j\,rms}}{U_\infty}\right)^2 \qquad (4)$$

Where h is the height of the slot and $u_{j\,rms}$ is the rms velocity of the jet in the exit plane. The rms jet exit velocity is used in this case, as the time averaged exit velocity for a ZNMF jet is identically zero. The coefficient '2' is found in the definition as for every period of excitation fluid is both exhausted and entrained through the orifice with an average velocity of $u_{j\,rms}$. It is noted that the characteristic momentum of the freestream used in this group, cU_∞^2, has no physical meaning. A normalising momentum based on the momentum thickness of the boundary layer, rather than the chord length, would perhaps be more appropriate. However, as the momentum thickness of the boundary layer was unknown, and would change as the angle of attack of the airfoil was altered, it was decided that the simpler definition would be retained.

An alternative non-dimensional measure of the relative strength of the ZNMF jet exhausting into the flow field is the velocity ratio:

$$VR \equiv \frac{u_{j\ rms}}{U_\infty} \qquad (5)$$

This alternative measure was used to establish whether the jet momentum or the jet velocity was of greater significance in determining the effectiveness of the ZNMF jet in controlling the separated flow.

5.0 EXPERIMENTAL APPARATUS

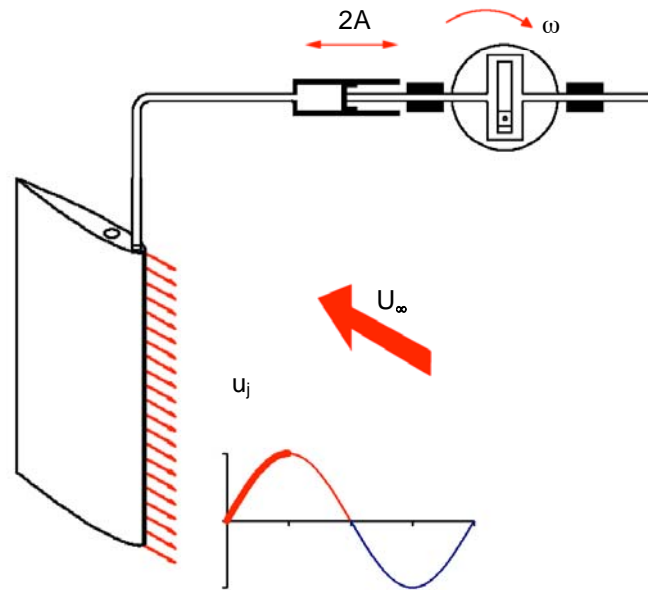A general schematic of the experimental setup is shown in figure 5.1.

Figure 5.1 – Schematic of Experiment

In this investigation an airfoil was mounted vertically within a water tunnel. A 2-dimensional slot, oriented normal to the surface at the leading edge, extended the entire span of the airfoil. Pressure oscillations were supplied to a cavity behind this slot, which resulted in a ZNMF jet exhausting from the leading edge slot. These pressure oscillations were supplied by an excitation system that consisted of a stepper motor connected to a piston/cylinder arrangement via a scotch yoke mechanism. Other experimental apparatuses used throughout the investigation included a dye supply system, imaging equipment and lasers used to illuminate planes within the flow. A more detailed description of the individual apparatus appears in the forthcoming sections.

5.1 WATER TUNNEL FACILITY

All experiments performed in this investigation were conducted in a closed circuit, horizontal water tunnel. Water was used as the working fluid in these experiments as by virtue of its lower kinematic viscosity when compared to air, velocities (and hence characteristic frequencies) a factor 18 lower are inherent for the same Reynolds number flows. This affords for much more relaxed acquisition and excitation timescales.

The water tunnel had a 5m long test section with a cross sectional area of 500mm x 500mm. Experiments were performed at various locations within the test section. A 53kW electric motor coupled with a centrifugal pump drove the water tunnel. The freestream tunnel velocity was adjusted by controlling the speed of the motor. This was achieved using a Sami GS frequency controller, which allowed the tunnel velocity to be set in increments of approximately 1.4 mm/s.
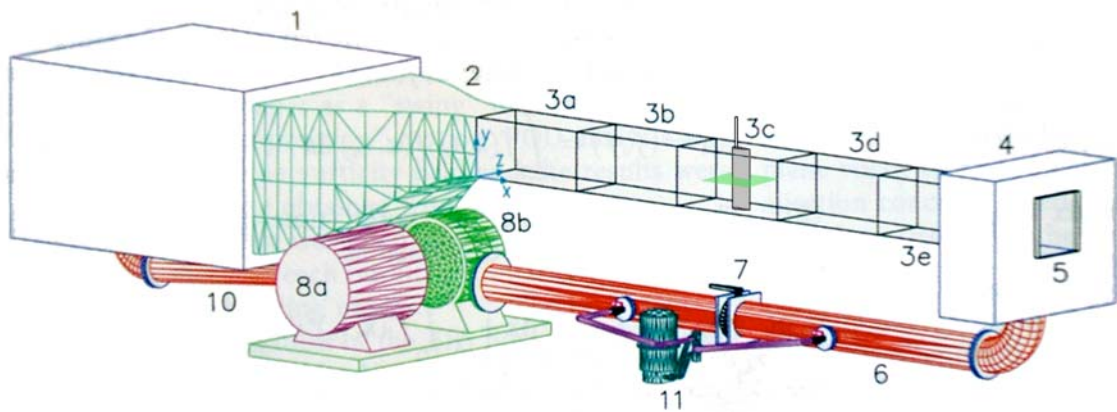
Figure 5.1.1 – Water tunnel facility. Image adapted from Kostas, Soria and Chong, 2002.
1: Settling Chamber, 2: 10:1 Contraction, 3: Test Section, 4: Plenum Chamber, 5: Rear Observation Window, 6: Return Pipework, 7: Filtration Isolation Valve, 8: AC Motor and Centrifugal Pump, 10: Return Pipework (pressure side), 11: Filtration Circuit.

A large settling chamber existed upstream of the test section. The pump flow was introduced into the settling chamber through a large perforated pipe that uniformly distributed water into the rear of the settling chamber. A series of four stainless steel screens of decreasing mesh size and a honeycomb section were inserted into the settling chamber in order to ensure flow uniformity. The honeycomb section exists between the first and second screens to straighten the flow and remove any mean swirl (Kostas et al, 2002). A 10:1 contraction existed between the settling chamber and the test section of the water tunnel. This contraction accelerated the mean flow, thereby reducing the turbulence intensity of the test section freestream. The flow screening and contraction devices resulted in a freestream turbulence intensity of less than 0.1%. Such a low level of turbulence intensity is ideal, and indeed required, for active flow control experiments in order to isolate the control effects from those induced by turbulent oscillations in the freestream.

Following the test section, the flow entered a plenum chamber by passing through perforated stainless steel plates oriented parallel to the test section walls. This arrangement was used as it resulted in the minimum possible disturbance to the upstream test section flow. The flow returned to the pump from the plenum chamber via a 300mm diameter pipe. Also included in parallel to the return pipe was a filtration system that was used to remove particles used for PIV experiments from the system.

Figure 5.1.1 shows a schematic of the water tunnel facility used in this investigation. Superimposed on the schematic is the airfoil in the orientation used throughout the experiments. The plane from which all of the flow characterisation images were collected is highlighted in the schematic.

5.2 AIRFOIL GEOMETRY

A Perspex airfoil with a NACA 0015 profile, a chord length of 100mm and a span of 510mm was used throughout this investigation. A NACA 0015 profile was chosen for a number of reasons. Firstly, it was determined that a symmetric airfoil would be most appropriate due to the fact that symmetric airfoils generate zero lift force at an angle of attack of 0°. This property would allow for a relatively simple method through which the zero angle of attack position for the airfoil could be set. Secondly, a NACA 0015 airfoil was used in experiments by Seifert et al (1996) and hence a set of

baseline measurements on this profile was readily available for comparison purposes. The final reason for the choice of a NACA 0015 profile was the increased rigidity offered by the use of a relatively thick airfoil.

A full-span slot with an average height, h, of 0.15mm (0.15%c), oriented normal to the surface at the leading edge, was manufactured into the airfoil as shown in figure 5.2.1. This slot height relative to the airfoil chord is narrower than slots used in previous research; for example Seifert et al (1993, 1996) used slots of between 0.3-0.4%c, Donovan et al (1998) used an excitation slot of 0.5%c and Wu et al (1998) simulated an excitation with a relatively large width of 2.5%c.

The slot height was chosen to be as narrow as possible so that the jet exit velocity was maximised for a given displacement of fluid. After manufacturing techniques were taken into consideration this was determined to be nominally 0.1mm. The narrowest slot possible was decided upon as for the same displacement of fluid the jet exit velocity was maximised. It was postulated that greater jet exit velocities would result in stronger vortices being formed by the ZNMF jet. Stronger vortices were assumed to in turn result in a more effective control of the separated flow field. Another motivation for choosing the narrowest possible slot came from considerations of scaling the control system to a full-scale aircraft. For example a slot of 1% chord over a commercial airliner chord length of 5m would result in a 50mm slot; quite an impediment on the structure of the wing and also on the flow field. However, a slot of 0.15%c as used in this study would present a significantly less intrusive slot of height 7.5mm.

It was desired that the slot be as close as possible to the separation point, as previous research has indicated that the most beneficial results are obtained when excitation is located close to the separation point. However, the separation point for
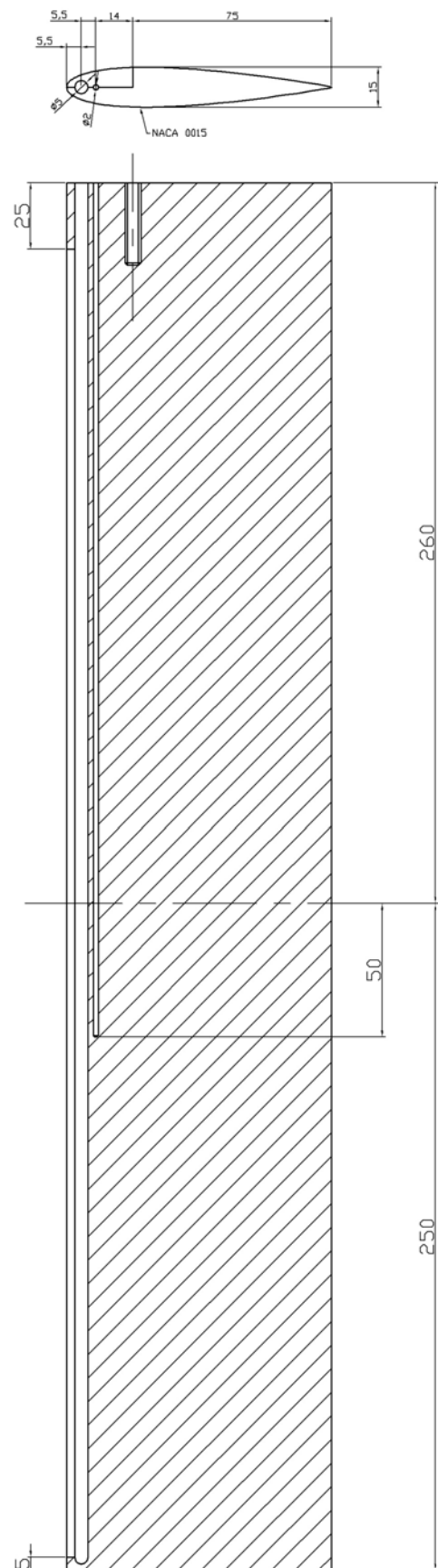

Figure 5.2.1 – Airfoil detail drawing

the airfoil was not known and was likely to change as the angle of attack of the airfoil was altered. Active flow control was expected to be most effective at angles of attack greater than the stall angle, where the separation point for most airfoils is at or very close to the leading edge. Hence, locating the slot at the leading edge was considered to be a close approximation to the optimum location.

The airfoil was manufactured using a computer controlled milling machine. Initially, the leading edge quadrant shown in figure 5.2.1 was cut out of the raw Perspex. This allowed the internal holes to be created using a spherical end cutter. The leading edge quadrant was then replaced, with a layer of double sided tape (of nominal thickness 0.1mm) placed between the two parts of the airfoil. This tape was placed all around the contacting surfaces except at the leading edge, where a nominally 0.1mm gap was created. The leading edge quadrant was then screwed into position at 4 equidistant spanwise locations. A filler material was placed over the screw heads such that the airfoil surface was smooth and continuous.

The leading edge slot was terminated 5mm above the airfoil base and slightly below the free surface of the water tunnel. This was done to ensure that air was not induced into the excitation system. The resulting total slot length was 460mm.

The slot height was nominally 0.1mm, however after all experiments had been completed the slot height was accurately measured in $^1/_{1000}$ inch increments using a set of feeler gauges. The spanwise variation in the slot height is presented in figure 5.2.2. A slot position of 0mm in figure 5.2.2 corresponds to the end of the slot closest to the top surface of the airfoil (that surface which protrudes above the free surface of the working fluid). As can be seen in figure 5.2.2 the slot has expanded slightly in the region between the screws used to secure the leading edge quadrant to the main airfoil section. This expansion has been caused by internal pressure within the 5mm diameter hole forcing the leading edge quadrant to deform slightly. Swelling of the Perspex due to water absorption would have also led to forces resulting in deformations of the leading edge quadrant, and hence expansion of the slot.
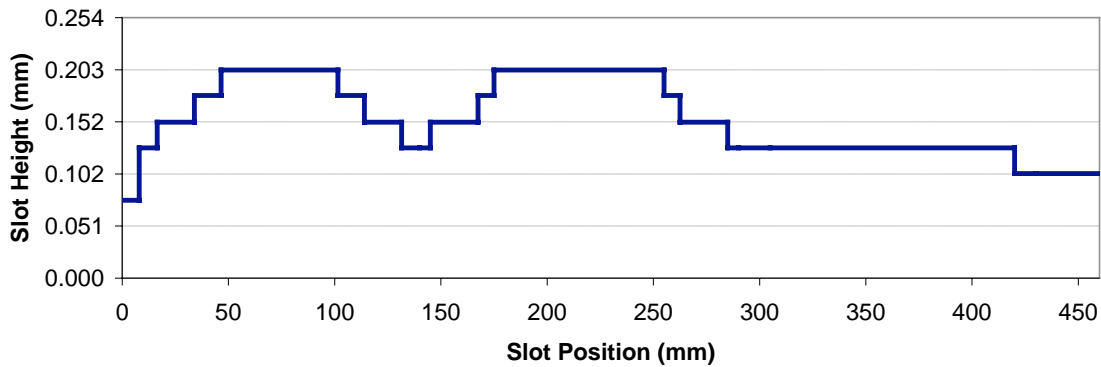

Figure 5.2.2 Spanwise variation in slot height

Pressure oscillations required to generate the ZNMF jet were supplied to the slot by a 5mm diameter hole. This hole ran the full spanwise length of the airfoil and was located at a distance behind the leading edge such that the slot was 3mm in chordwise length. In order to reduce the stresses forcing the leading edge quadrant to separate from the rest of the airfoil a stainless steel tube was inserted within the 5mm hole. A 1mm slot was machined along the length of the tube so that fluid could escape from the tube and out of the leading edge slot. Four bridges existed across this slot in order to retain the structural integrity of the tube; these bridges were co-located with the leading edge quadrant screws and were 5mm in length.

Immediately behind the 5mm diameter hole a 2mm diameter hole, whose purpose was to introduce dye to the mid-plane of the airfoil, was included. Originally it was planned that dye would flow down the 2mm diameter hole and out a 0.5mm diameter surface hole located at the mid-plane. However, after testing the airfoil it was apparent that the 2mm dye hole and the 5mm pressure supply hole communicated. Although not its original purpose, this leakage was used during the PLIF experiments to introduce dye into the ZNMF jet orifice.

The airfoil was mounted using a 20mm diameter sting located at the ¼ chord position. The airfoil was mounted vertically in the test section such that the base of the airfoil maintained a slight clearance (2-5mm) with the base of the water tunnel. In this configuration the top of the airfoil protruded above the free surface of the working fluid at all times. This ensured that the flow field around the airfoil was free from 3-Dimensional effects due to tip vortices.
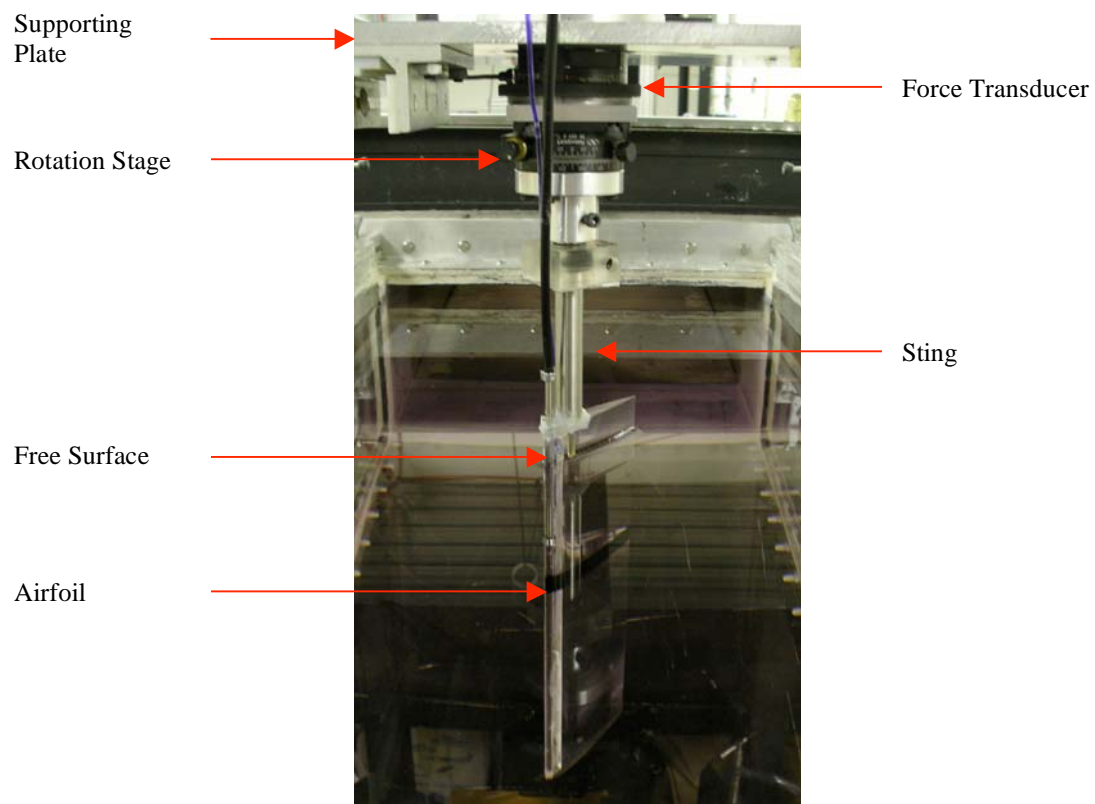

Figure 5.2.3 – Airfoil mounting arrangement.

The airfoil sting was secured to a micrometer rotation stage, which allowed the angle of attack to be measured with an accuracy of ±10 minutes. This rotation stage was fixed to a force sensor, which was in turn secured to the underside of the supporting plate. The supporting plate was mounted on a railing system that allowed the airfoil to be moved to any position along the water tunnel test section. Figure 5.2.3 shows the mounting arrangement used.

5.3 EXCITATION SYSTEM

Pressure oscillations were supplied to the 5mm diameter cavity within the airfoil in order to generate the ZNMF jet that issued from the leading edge slot. These

pressure oscillations were generated by the excitation system shown in figure 5.3.1. The excitation system consisted of a computer controlled stepper motor coupled to a piston cylinder arrangement via a scotch-yoke mechanism.
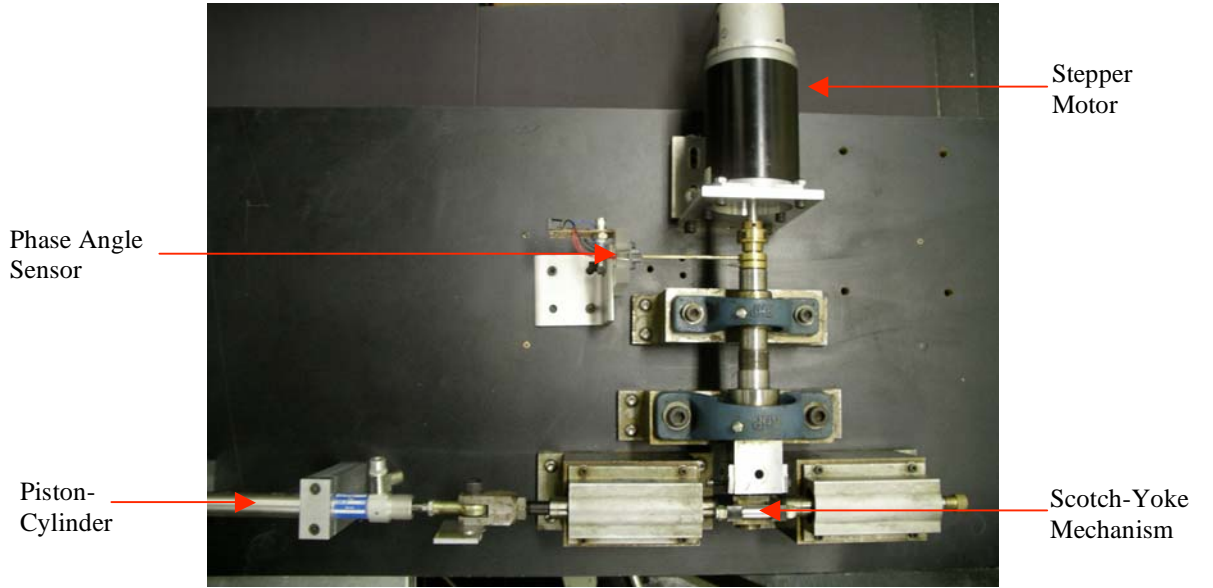

Figure 5.3.1 – Excitation system.

The frequency of the pressure oscillations was controllable by altering the rotational speed of the stepper motor using the commanding computer. Additionally, the amplitude of the piston translation could be adjusted by altering the crank length of the scotch-yoke mechanism. This crank length was continuously adjustable by varying the position of the constraining screws. Also included in the excitation system was a phase angle sensor. This sensor produced a 5V TTL level signal whenever the wand passed through the sensor location. Hence, one TTL level pulse was recorded for every excitation cycle and occurred at the phase position where the volume within the cylinder was at a minimum.

The piston used to create the pressure oscillations had a diameter of 20mm. The fluid displaced by the cylinder was ducted directly into the airfoil cavity through a nylon hose. This hose was designed to withstand extremely high pressures, and hence was assumed to be completely inflexible to the applied pressure oscillations.

Given the arrangement of the excitation system, a relationship between the jet velocity in the exit plane and the excitation parameters can be determined. Firstly, the rms piston velocity, $u_{p\,rms}$, is given by:

$$u_{p\,rms} = \frac{A\omega}{\sqrt{2}}$$

$$u_{p\,rms} = \frac{2\pi A f}{\sqrt{2}}$$

$$u_{p\,rms} = \frac{2\pi A F^{+} U_{\infty}}{\sqrt{2}c} \qquad (6)$$

Where A is the set amplitude of the scotch-yoke mechanism, ω and f are the rotational speed and frequency of the stepper motor respectively. The rms piston velocity can in turn be related to the jet velocity in the exit plane, $u_{j\,rms}$, as follows:

$$u_{j\,rms} = \frac{A_p}{A_j} u_{p\,rms}$$

$$u_{j\,rms} = \frac{A_p}{hL} \frac{2\pi AF^+ U_\infty}{\sqrt{2}c} \qquad (7)$$

Where A_p and A_j are the cross sectional areas of the piston and the jet (in the exit plane) respectively, h is the slot height and L is the slot length. The oscillatory momentum blowing coefficient can now be defined in terms of the system geometry as:

$$c_\mu \equiv 2\frac{h}{c}\left(\frac{u_{j\,rms}}{U_\infty}\right)^2 \qquad (4)$$

$$c_\mu = 2\frac{h}{c}\left(\frac{\dfrac{A_p}{hL}\dfrac{2\pi AF^+ U_\infty}{\sqrt{2}c}}{U_\infty}\right)^2$$

$$c_\mu \equiv \frac{4\pi^2 A_p^{\,2}}{hL^2 c^3}A^2 F^{+2} \qquad (8)$$

The relationship (8) was used for the calculation of all the oscillatory momentum blowing coefficients in this investigation. It is important to note that equation 8 assumes that the working fluid is incompressible, a perfectly reasonable assumption to make when working with water. It is also assumed that no crevice losses occur. Possible sources of crevice losses in this investigation include losses from the seal between the piston and the cylinder and losses through joins between the leading edge quadrant and main body of the airfoil.

5.4 FORCE TRANSDUCER

The airfoil was mounted on an ATI Industrial Automation Force/Torque 6-axis force transducer as shown in figure 5.2.3. The sensor worked on a Maltese cross principal and used silicon strain gauges to measure the forces acting on the sensor. The force transducer was connected to a stand-alone controller that digitised the amplified analogue strain gauge data. The digitised data was transferred to the monitoring computer via an RS-232 serial cable.

The force sensor had the capability to measure all 3 force components as well as the 3 moment components acting on the transducer. In this study only the two force components parallel and perpendicular to the freestream, the lift and the drag forces, were recorded. The resolution of the force sensor for the lift and drag forces was 0.1N. The maximum resolvable force was 130N, which was many times greater than the maximum force exerted on the sensor by the airfoil.

The resolution of the force sensor can be expressed in terms of the lift coefficient for a freestream velocity of 309 mm/s, which was the freestream velocity that was used for most of the force measurements. Using this velocity, a density of 1000 kg/m^3, and the airfoil reference area the resolution of the force sensor was determined to be $\Delta c_L = 0.042$. This resolution was just adequate for the studies that were undertaken, however some difficulties were encountered in trying to determine the dependence of parameters that produced only minor variations in the lift force.

The standard software supplied with the force sensor output data to the screen only and hence was insufficient for this application. The software was therefore modified to write the output data to an ASCII file as well as to the screen. Further software was also written to decipher the output file and calculate ensemble averages and standard deviations of a data stream. Appendix A contains a copy of the source code written for this application.

In its standard configuration the force sensor output data records at a rate of approximately 20Hz. An option existed to increase this data transfer rate, however it was found that when this option was exercised the data stream became inaccurate. Unphysical jumps in the force history were detected when the output frequency of the transducer was increased and hence the standard transfer rate was retained throughout the study.

5.5 FLOW VISUALISATION DYE SUPPLY

Dye was supplied for the flow visualisations using a Mariotte bottle, 'a device that provides a constant effusion velocity for liquids,' (Maroto, J., de Dois, J. and de las Nieves, F., 2002). A Mariotte bottle was used since a constant outflow velocity, independent of the fluid level in the reservoir, allowed for different experiments to be compared directly. The outflow velocity was regulated using a finely incremented micro-valve that allowed the outflow velocity to be set with a high degree of repeatability. A schematic of a Mariotte bottle with a micro-valve attached is shown in figure 5.5.1.
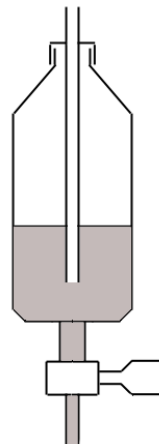
Figure 5.5.1 – Mariotte bottle with micro-valve attached.

The Mariotte bottle was mounted approximately 1m above the free surface of the water tunnel for dye streak flow visualisations. For PLIF experiments it was found that more head was required and hence the Mariotte bottle was relocated to a position 1.5m above the free surface of the water tunnel.

5.6 PHOTOGRAPHIC EQUIPMENT

Two different digital cameras were employed throughout this investigation. For the dye streak flow visualisations a Fujifilm S2 pro digital SLR camera was used. This camera had a maximum CCD output resolution of 12.1 megapixels and was capable of capturing 7 images in quick succession, with a time lag of approximately 1 second between exposures.

For the PLIF and PIV elements of the study a PCO Pixelfly monochrome camera was used. This camera had the advantage of being able to be triggered from an external source and was capable of capturing images at a much faster frame rate of approximately 12fps. This frame rate could be doubled if binning was employed, however this option was not utilised in order to maintain the maximum image resolution. At full resolution the Pixelfly camera produced a 1280 x 1024 pixel image with a 12-bit color depth.

5.7 LASERS

A dual cavity New Wave Research Gemini PIV Nd:YAG laser was employed for the PLIF experiments. Each laser was capable of producing a 6ns 200mJ pulse of wavelength 532nm at a repetition frequency of 10Hz. A set of collimating lenses transformed the laser pulse into a sheet approximately 2mm thick and 300mm wide.

The laser sheet intersected the test section in a plane located 289mm above the base of the water tunnel. This plane corresponded to a location 226mm from the top surface of the airfoil. This was not the mid-plane of the airfoil as was ideally desired, however was offset from this plane by 29mm. The reason for this offset was that other experiments, requiring the described laser sheet location, were being conducted concurrently using the same apparatus. As the flow field around the airfoil was ideally 2-Dimensional, negligible discrepancy should have existed between this plane and the mid-plane of the airfoil.

The firing of the lasers as well as the triggering of the camera was controlled using real-time Linux. An unavoidable 180 μs delay existed between the output signal of the real-time Linux system and the firing of a laser pulse.

6.0 EXPERIMENTAL PROCEDURE

6.1 FORCE MEASUREMENTS

The general approach that was followed for this phase of the study was as follows. Initially, the airfoil lift curves were measured for a wide range of jet frequencies and momentums. From these curves a narrower range of the most promising forcing frequencies and momentums was determined and studied more systematically. Firstly, the jet momentum was held constant and the excitation frequency was varied. Secondly, the excitation frequency was kept fixed and the jet momentum was varied. For this more specific segment of the force measurements only angles of attack between 15-20° were considered, as it was previously determined that the greatest increase in lift coefficient was found around these angles. The optimum forcing conditions, defined as the conditions that resulted in the greatest lift increments, were determined. These forcing parameters were applied and the characteristics of the optimum controlled airfoil were measured and compared to those of the uncontrolled airfoil.

Before any force measurements were undertaken the principal axis of the force transducer was aligned with the freestream direction of the water tunnel. Originally it was planned to use a cylinder submerged in the freestream to align the transducer. As a stationary cylinder produces only a drag force, the output of the force transducer could be used to ensure that the principle axis of the force transducer was aligned with the freestream. However, it eventuated that the resolution of the force sensor was not fine enough to accurately resolve the drag component of any available cylinders. Hence the force sensor was aligned geometrically with the walls of the test section.

The following procedure was used to obtain all the force measurements recorded throughout the investigation. Initially, the tunnel and filtration system were both switched off. No measurements were taken until at least 20 minutes after the tunnel was stopped in order to ensure that any residual motion of the fluid within the test section had completely dissipated. Baseline force measurements were obtained with the airfoil mounted in exactly the configuration that was to be used for subsequent testing. These baseline measurements were obtained for all angles of attack that were to be considered once the experimental freestream velocity had been set.

The baseline measurements obtained were plotted and a trendline fitted to them. In all cases the baseline force measurements were linear or only slightly curved with respect to angle of attack. Reference force measurements were derived from the trendline data rather than the raw data. This was done as with no freestream velocity the only forces and torques acting on the transducer were those due to the weight of the airfoil and the connections to the external pressure and dye hoses. These forces should all vary smoothly and continuously with respect to angle of attack and hence any deviations from a smooth profile can be confidently attributed to sensor noise. Removal of sensor noise using a trendline process served to decrease the random error in the net results.

Following the collection of reference forces the tunnel was set to the desired freestream velocity and was allowed a further 20 minutes to ensure that the freestream had fully settled at the desired speed. Force measurements were then obtained at the forcing conditions and angles of attack to be tested. In the preliminary investigations force measurements were only collected for ascending angles of attack, however for the final force measurements, once the optimum forcing parameters had been determined,

force measurements were collected for both ascending and descending angles of attack. This was undertaken in order to account for any hysteresis in the results.

Freestream velocities of 309mm/s and 398mm/s, which corresponded to Reynolds numbers of 3.08 x 10^4 and 3.96 x 10^4, were used for the force measurements. 398mm/s was the first velocity chosen; this velocity was close to the maximum repeatable freestream velocity that could be obtained in the water tunnel. The highest velocities possible were employed in order to maximise the forces acting on the airfoil. This in turn resulted in the percentage resolution error of the force sensor being minimised. Later testing at higher jet momentums was conducted at a lower freestream velocity of 309mm/s. The freestream velocity was reduced in order to reduce the momentum of the jet and hence the pressure in the ZNMF jet cavity. This was undertaken as concerns were raised as to the deformation of the slot due to the pressure forces within the cavity.

The lift and drag coefficients were determined from the difference in the force measurements as demonstrated in equation (9).

$$c_L = \frac{F_{U_\infty} - F_{U_o}}{\frac{1}{2}\rho U_\infty^2 S} \qquad (9)$$

Where F_{U_∞} and F_{U_o} are the cross-stream force measurements obtained with the experimental freestream velocity and with zero freestream velocity respectively. S is the planform area of the airfoil and was determined from the chord length and measurement of the span of the airfoil that was submerged under the water. The exact span of the submerged airfoil was determined at the trailing edge of the airfoil when the airfoil was set at zero degrees angle of attack with the tunnel velocity set at the experimental freestream velocity. An identical method to that specified in equation (9), however using the streamwise force components, was used to determine the drag coefficient.

All force measurements collected were ensemble averaged over 500 samples obtained from the force transducer. The standard deviation of the sample was also noted. 500 samples was chosen to be a sufficient period for the measurement of the forces as this corresponded to the forces being averaged over a time period of 25 seconds. This period was many times longer than the periods of any of the flow frequencies expected to be encountered, and hence any time dependence would be accurately averaged.

Once the lift and drag coefficients had been calculated the angle corresponding to 0° angle of attack was determined. This was defined as being the angle for which the measured lift coefficient for the uncontrolled airfoil was zero. As the airfoil used was symmetric, this condition corresponded to the airfoil chord-line being aligned with the freestream.

6.2 DYE STREAK FLOW VISUALISATIONS

For dye streak flow visualisations 'Bluo,' a blue tinted laundry bleach was used. A bleach based dye was used as it is inorganic and hence does not stimulate the growth of algae and bacteria within the water tunnel.

The dye was introduced through a 2.5mm diameter tube mounted 77mm upstream of the leading edge of the airfoil. The end of the dye tube was bent at 90° such that dye was released parallel to the freestream. In order to avoid vortices shedding from the dye tube and disturbing the downstream flow the tube was mounted

inside a streamlined section of model aircraft strut tubing. This tubing resembled a symmetric airfoil profile with a maximum thickness of 6.75mm. The dye tube was located within the water tunnel at a height that allowed the dye to be released at the mid-plane of the airfoil.

In order to minimise perspective distortion between the base and mid-plane of the airfoil, the camera was moved to a distance of approximately 2.75m away from the base of the airfoil. Had the camera not been moved far afield the out of focus base of the airfoil would have obscured the view of the mid-plane. Moving the camera far afield required the use of a zoom lens to focus the CCD array only on the region of interest. A 105mm focal length Micro-Nikkor lens was used in conjunction with a 2x tele-converter to provide the necessary focal length of 210mm.

The region of interest was imaged from below using a mirror oriented at 45° to the freestream direction, as there was not sufficient space beneath the water tunnel to image the airfoil directly from the required distance.

The flow-rate of dye was adjusted such that the dye issuing from the end of the tube did not form a distinct jet or wake flow. The smooth release of dye from the end of the tube indicated that dye exit velocity was approximately matched with the freestream velocity. The micro-valve setting corresponding to this condition was recorded and all experiments were conducted with an identical dye flow-rate.

Images were collected at random time and phase intervals for the uncontrolled and the optimum controlled conditions at an angle of attack of 18° and a freestream velocity of 154mm/s. Images were recorded using the continuous shooting mode of the camera. These images were considered both individually and in an averaged sense.

6.3 PLANAR LASER INDUCED FLUORESCENCE

For the PLIF investigation the mariotte bottle was filled with Kiton Red 620 fluorescent dye. This dye fluoresces with a wavelength of 620nm when exposed to laser radiation with a wavelength of 532nm (Cater and Soria, 2002). The dye was introduced into the 2 mm diameter hole in the airfoil. Due to the communication between the internal cavities discussed earlier, the dye mixed with the fluid in the pressure supply cavity of the ZNMF jet. Hence, dye was subsequently ejected into the flow field during each forcing stroke of the jet.

The addition of a constant mass flow of dye to the jet violates the zero-net-mass-flux condition imposed on the jet. The jet now has a constant, albeit small, time averaged net mass flow. The additional mass flow added to the ZNMF jet cavity was not quantified, however it was assumed to be negligible relative to the total mass flux through the jet orifice. The additional volume was assumed to be small enough that it would not have any detectable affects on the global flow field.

In this phase of the study the Pixelfly camera was used in conjunction with a 105 mm Micro-Nikkor lens. A red filter was attached to the end of the lens. This filter was required as laser light scattered off the airfoil and particles within the working fluid as well as causing the dye to fluoresce. The addition of the red filter ensured that only the fluorescing of the dye was captured on the CCD array.

The signal from the phase angle sensor included in the excitation system was fed into a real-time Linux program that synchronized the firing of the lasers and the camera. The program allowed for a fixed time delay between the input signal and the output

signal to be defined. As the phase angle signal was fixed at a particular phase location, this time delay was used in order to trigger the lasers and camera at any other point during the excitation period. The software parameters were set such that one trigger signal was sent to the camera and the lasers for every excitation period.

The time delay between the phase angle wand passing through the sensor and the exposure of the image on the camera was evaluated before any experiments were completed. This was achieved by focusing the camera on the phase angle sensor and triggering it with zero time delay. The image of the phase angle wand showed that it was within the sensing location; this indicates that a negligible time delay existed between the phase angle sensor registering a signal and the camera firing. Hence for all subsequent experiments it was assumed that this time delay was identically zero.

It was found that the largest laser intensity possible was desired, as only a small amount of dye managed to seep into the ZNMF jet cavity. The use of larger laser intensities maximised the fluorescence of the small amount of dye that was available. In order to increase the overall laser energy without increasing the instantaneous intensities to levels that may have damaged the Perspex tunnel walls, a double pulse (one pulse from each laser cavity in quick succession) was used. Due to the 180μs delay between the signal being sent to the laser and the laser firing, the shortest time delay that could be used was approximately 200μs. This time delay was employed along with a camera exposure time of 400μs. This configuration allowed fluorescence due to both laser pulses to be captured by the CCD array.

Instantaneous PLIF images were acquired in a continuous fashion until the computer memory limit was exhausted. Phase specific and random phase averaged images were also acquired. These averaged images were the average of 64 individual images. Images were collected at an angle of attack of 18° for the uncontrolled and optimum controlled conditions. The images were obtained at a freestream velocity of 154 mm/s, which corresponded to a Reynolds number of 1.54×10^4. No phase reference was available for the uncontrolled case; hence images collected for this case were not phase specific. It may have been possible to phase lock the images of the uncontrolled airfoil to the leading edge shedding frequency. This would have required the use of a hot-film or other similar device to be inserted within the leading edge shear layer to act as a trigger for the image acquisition system. The focus of this study was not to accurately investigate the mechanics of the uncontrolled airfoil, and hence it was deemed beyond the scope of the study to phase lock the uncontrolled airfoil flow field.

Instantaneous and averaged phase specific images were however obtained for the controlled airfoil. The phase specific images were acquired at phase angles of 0°, 45°, 90°, 135°, 180°, 225°, 270° and 315°. A phase angle of 0° corresponded to a phase location where the expulsion of fluid from the ZNMF jet orifice had just concluded.

After the images had been captured they were digitally enhanced using a spectrum spreading technique. The airfoil outline was overlaid on the images to allow the viewer a point of reference.

7.0 RESULTS AND DISCUSSION

7.1 FORCE MEASUREMENTS

7.1.1 PRELIMINARY FORCE MEASUREMENTS

The uncontrolled airfoil lift curve was measured and is displayed in figure 7.1.1. The experimental data presented was derived from the average of 9 individual lift curves, which include curves derived from both increasing and decreasing angles of attack. The experimental data is compared to the uncontrolled lift coefficient curve for a NACA 0015 airfoil as determined by Seifert et al (1993). The comparison data was collected at a Reynolds number of 0.15×10^6, whist the experimental data was collected at much
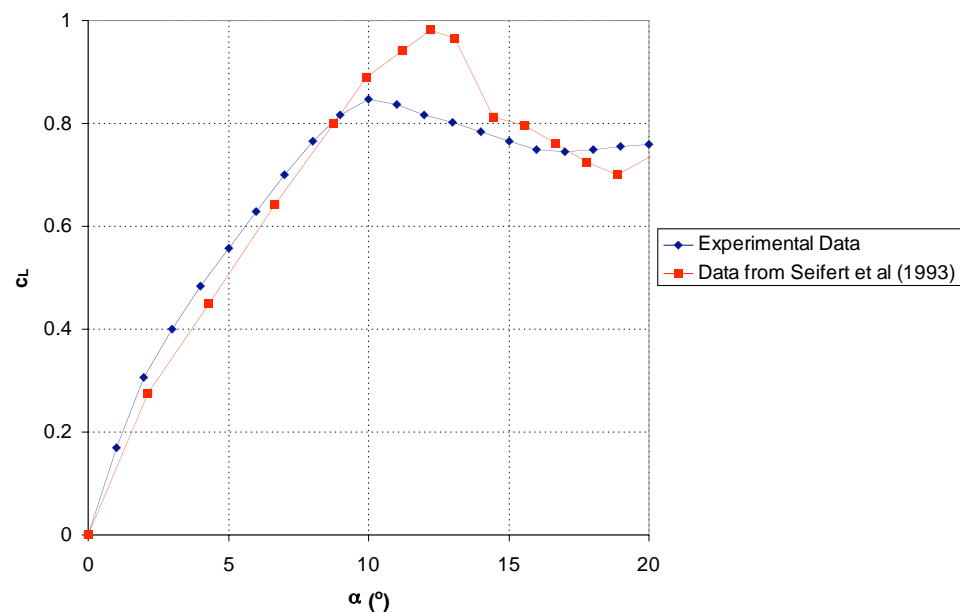
lower Reynolds numbers in the range of $3\text{-}4 \times 10^4$.

Figure 7.1.1 – Comparison of uncontrolled lift coefficients

A clear discrepancy in the airfoil stall angle and stalling characteristic is evident from figure 7.1.1. The experimental data and the comparison data are in reasonable agreement for angles of attack lower than the stall angle and for angles of attack in the deep-stall region. There are however marked differences in the airfoil performance around the stall angle.

The experimental data suggests a gentle stall occurring at an angle of attack of 10°, whilst the data of Seifert et al suggests a much sharper stall at an angle of attack of 12°. Two separate explanations for this discrepancy exist. The first explanation centres on the difference in the Reynolds numbers at which the data was collected. The experimental data, collected at a lower Reynolds number, was likely to have exhibited laminar boundary layer separation. Characteristics of a laminar separation are a lower stalling angle, and by virtue of the reduced maximum lift coefficient, a reduced severity of the stall. As the comparison data was determined for a much higher Reynolds number, the laminar separation effects would not have been as pronounced.

The second possible explanation for the lower stalling angle is the effects of tunnel blockage. Table 7.1.1 shows the frontal area of the airfoil and the percentage of the cross-sectional area of the water tunnel that was blocked by the airfoil for a range of angles of attack.

| α (°)	Airfoil Frontal width (mm)	Tunnel area blocked (%)
0	15	3.0
10	21.6	4.3
15	29.2	5.8
20	36.9	7.4
30	51.85	10.4

Table 7.1.1 – Tunnel Blockage

As can be seen in table 7.1.1 at angles of attack around the stall angle tunnel blockages in the order of 5% of the tunnel cross-sectional area were experienced. This magnitude of blockage leads to significant local increases in the flow velocity around the airfoil and the possibility of a premature stalling angle.

It is also noted in figure 7.1.1 that the gradient of the lift curve below the stall angle is not entirely constant. Thin airfoil theory predicts a linear lift curve for a flat plate for angles of attack up to the stall angle. All of the uncontrolled and controlled lift curves measured exhibited a greater lift coefficient gradient for angles of attack between $0°$ and $2°$ than for angles of attack greater than $2°$. The cause of this phenomenon was not fully explored, however was suspected to be due to the relative thickness of the airfoil used.

Figure 7.1.2 shows lift coefficient curves determined for non-dimensional frequencies of 0.3, 0.58, 1, 1.27, 1.6 and 2. For each non-dimensional frequency a range of momentum blowing coefficients between 0 (the uncontrolled case) and 0.08% were considered. Similar momentum blowing coefficients have been used for each of the 6 frequencies considered.

Some data spread due to drift in the force sensor was apparent in the experimental results. It could be said with some confidence that the effects were due to drift in the sensor and not fluid mechanic effects as at an angle of attack of $0°$ variation in the measured lift force was noted. However, at this angle, with the ZNMF jet located as it was at the leading edge, activation of the jet should have resulted in identical effects occurring on both the upper and lower surfaces of the airfoil. This, in turn, would have resulted in no net change to the lift coefficient as was suggested by the raw data. Hence, the lift forces were referenced by setting the lift coefficient to zero at an angle of attack of $0°$.

It can be seen in figure 7.1.2 that the excitation had little effect on the lift coefficient at angles of attack less than the uncontrolled stalling angle of $10°$. This observation is consistent with the findings of Seifert et al (1993, 1996) and Donovan et al (1998) who have also observed minimal lift increments for naturally fully attached flows. This suggests that the control requires the presence of a separated shear layer in order to have any influence the global flow field. Another conclusion that can be drawn from this observation is that the control must work by affecting the dynamics of the separated shear layer.

$F^+ = 0.3$
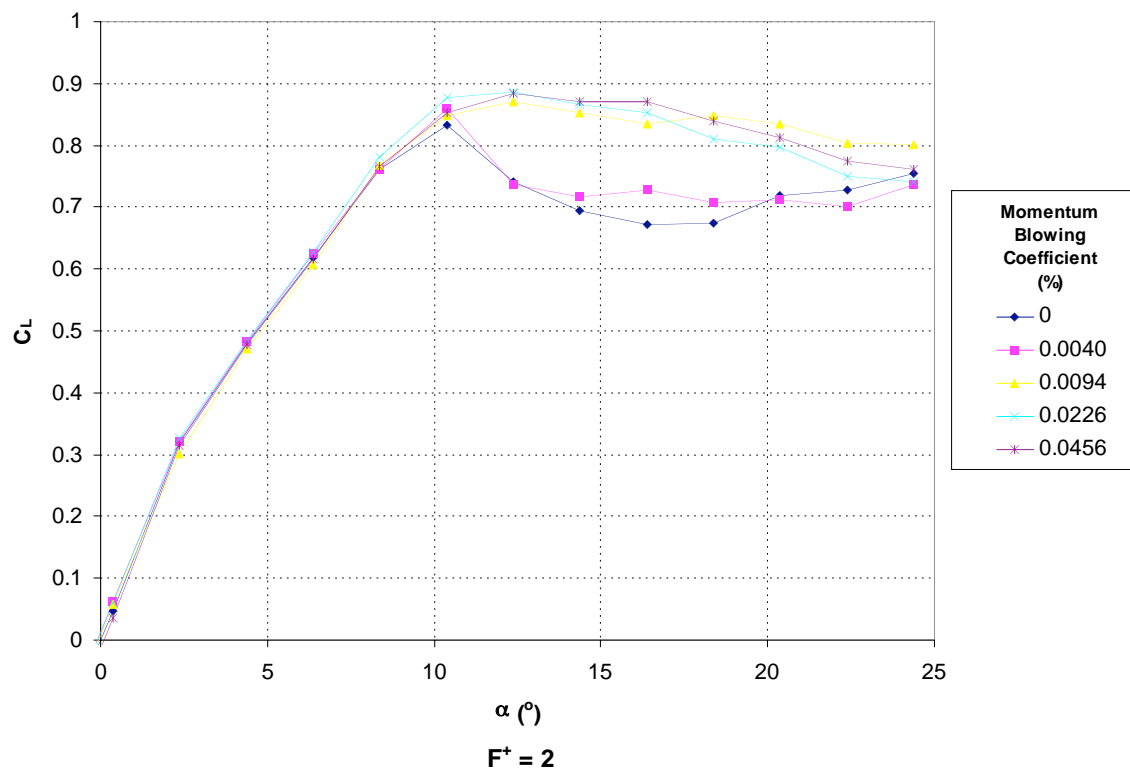

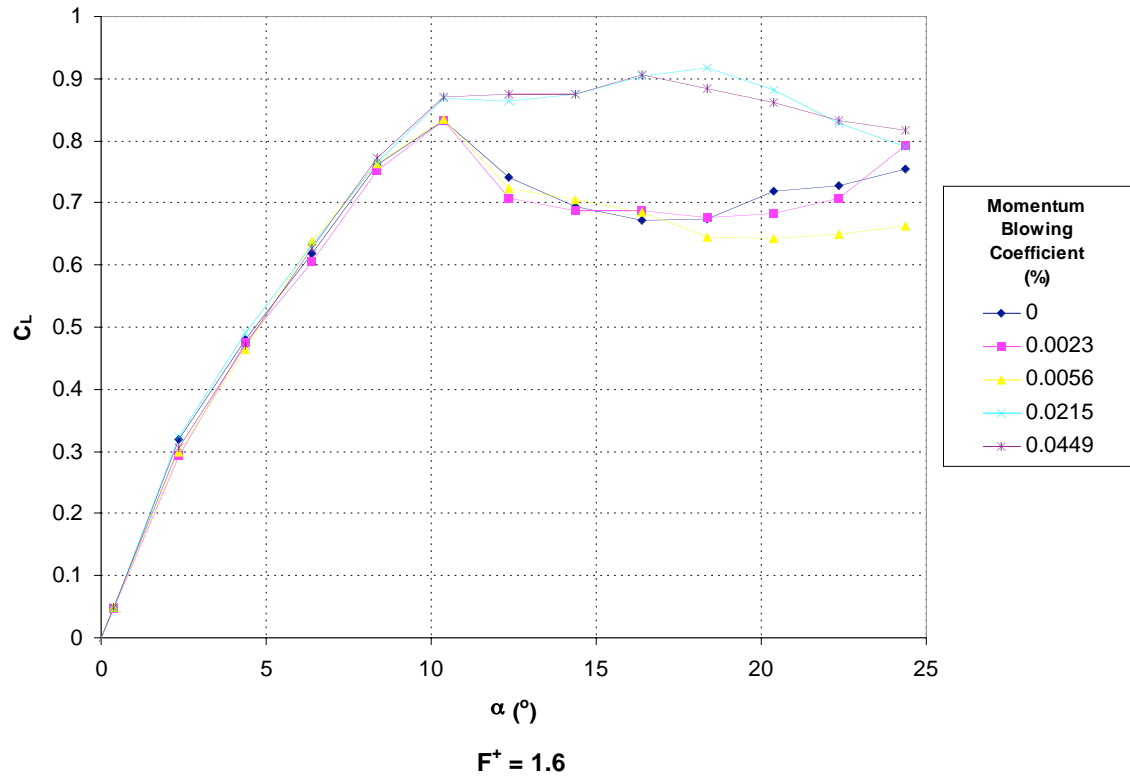$F^+ = 0.58$

$F^+ = 1$

$F^+ = 1.27$
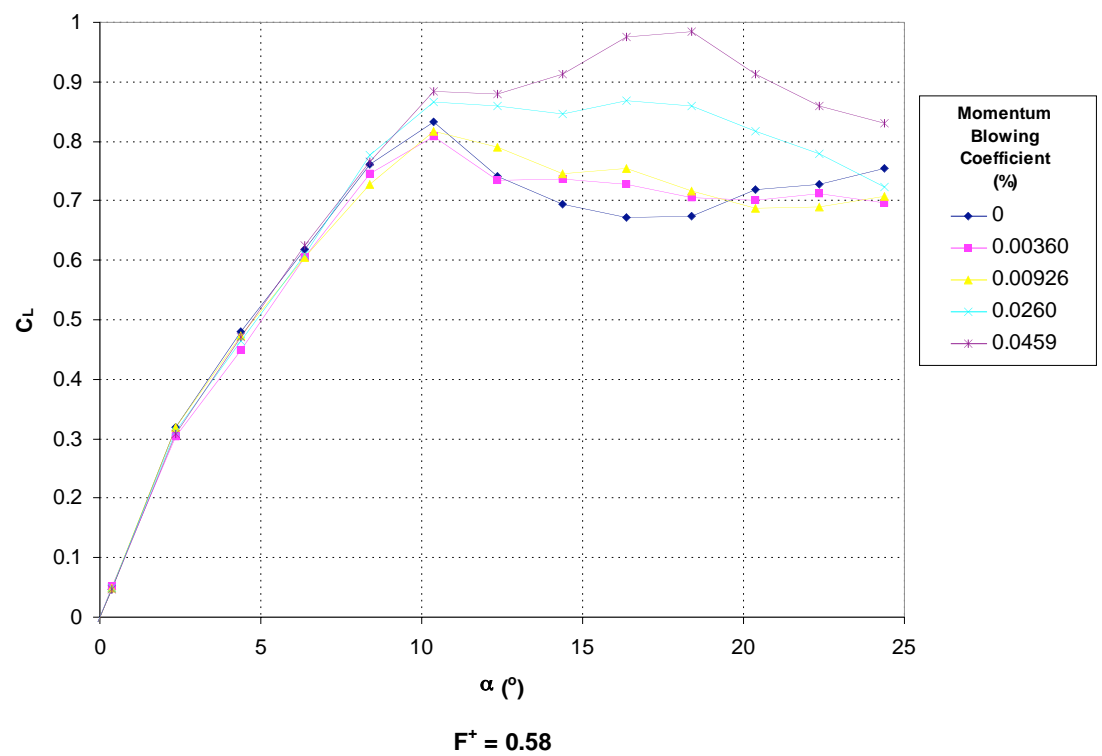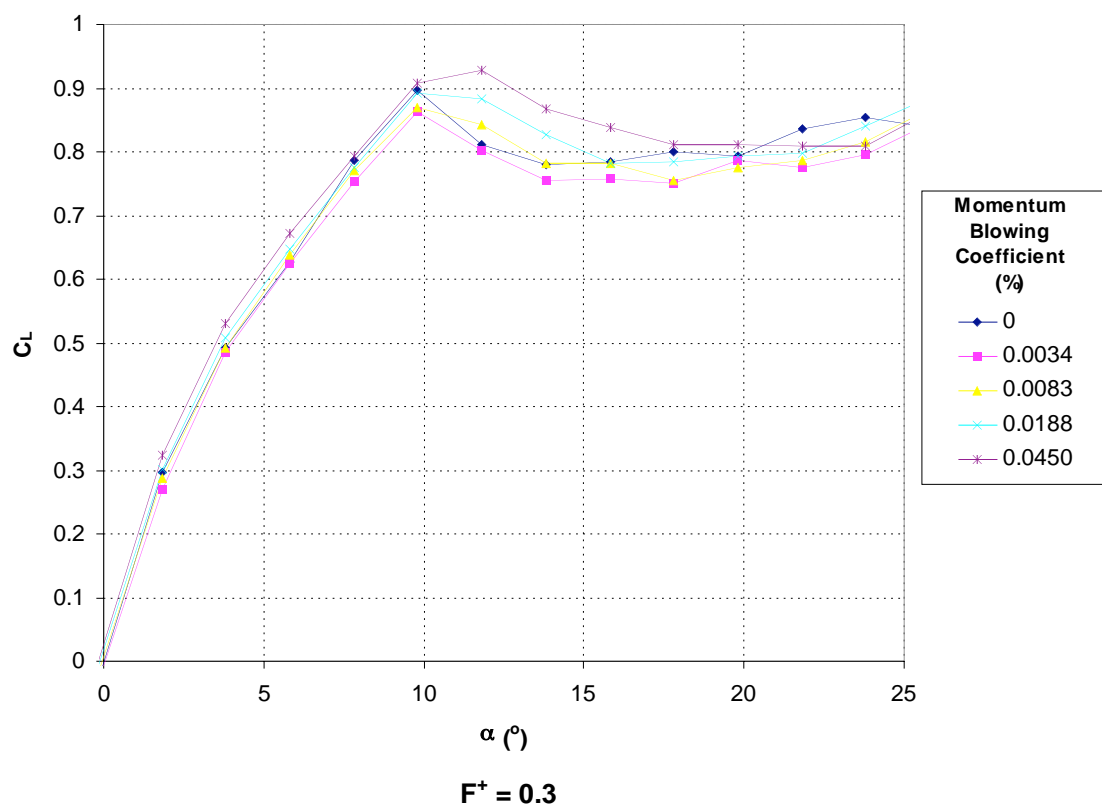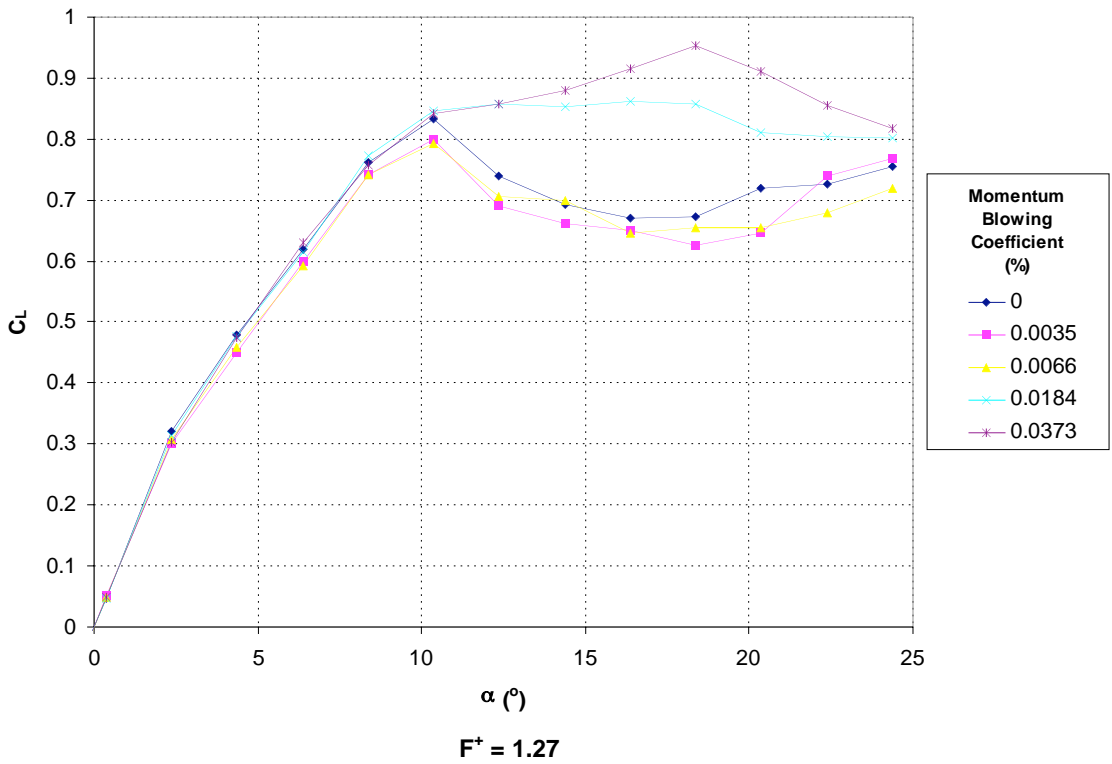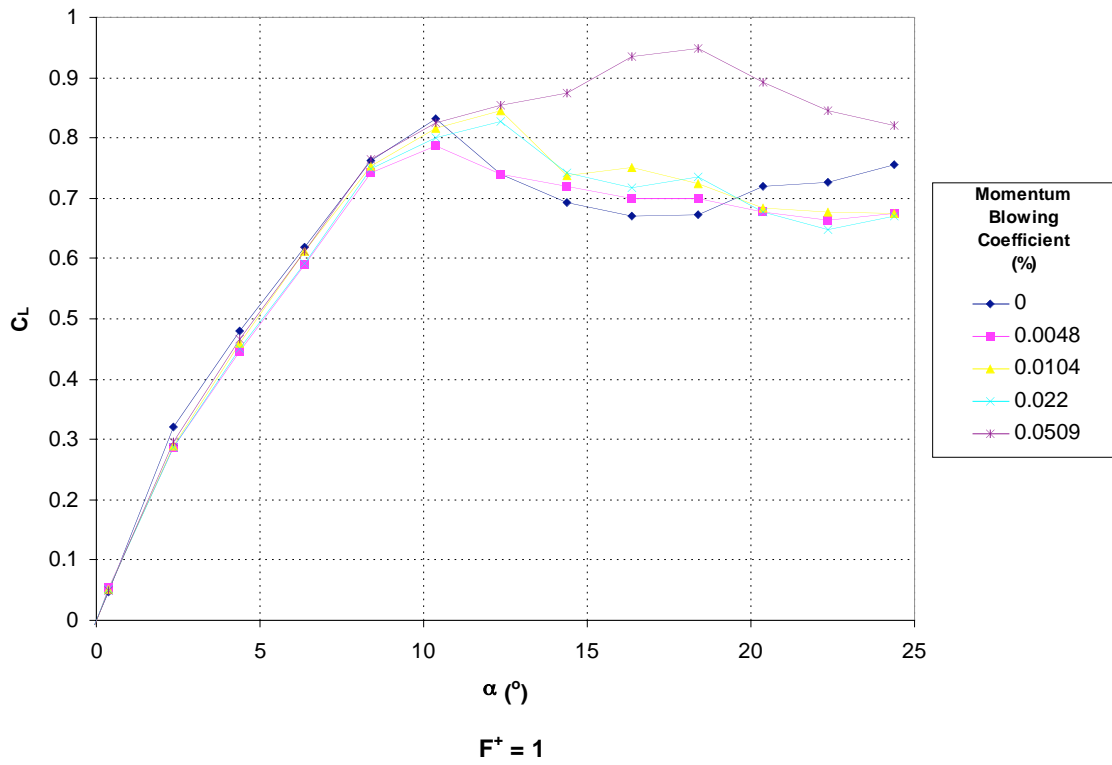
Figure 7.1.2 – Lift curves for a range of excitation frequencies and jet momentums.

It is seen from figure 7.1.2 that the maximum post-stall lift gains are achieved for non-dimensional frequencies of between 0.58 and 1.6. The extremes of the frequencies tested: $F^+ = 0.3$ and 2 resulted in lesser effectiveness of the excitation to increase the post-stall lift. It must however be noted that for momentum blowing coefficients less than 0.01% a non-dimensional frequency of 2 was the only frequency that resulted in lift increments greater than 10%. In fact at $F^+ = 2$ with $c_\mu = 0.0094\%$ maximum lift increments in the order of 25% were achieved. This suggests that higher frequencies may be more effective for low momentum excitation than lower frequencies, which appear to be more effective for higher momentum excitation.

For all frequencies considered, an oscillatory momentum blowing coefficient of less than 0.005% was found to be too weak to impart any significant change on the lift coefficient. As the jet momentum was increased above this level the post-stall lift increments were also increased. In many cases it appeared as if there was a threshold jet momentum required to affect any control on the flow. However, this is most likely a false impression due to the exponential distribution of jet momentums tested. For all frequencies less than $F^+ = 1.6$, the trend of the lift increments suggested that further lift gains could be realised by increasing the jet momentums to higher levels than those tested in this initial study.

At the highest jet momentums tested in this segment the greatest gains were found for non-dimensional frequencies of between 0.58 and 1.27. In this range, with the maximum momentum blowing coefficients investigated, the airfoil stall angle was seen to be mitigated from an angle of attack of 10° up to an angle of attack of approximately 18°. This in turn resulted in the post-stall lift coefficient being increased by between 40% and 46% at an angle of attack of 18.4°, with the peak gain being found for a non-dimensional frequency of 0.58.

Following this initial test, where a broad range of frequencies and amplitudes were considered, a more systematic approach was taken to identify the optimal frequencies and momentums required to effect post-stall flow control. Firstly, the most effective forcing frequency was identified by examining the range of $F^+ = 0.58$-1.27 in more detail. Following the identification of the optimum frequencies, the variation in the lift increment with respect to the jet momentum was investigated at these frequencies.

7.1.2 DEPENDENCE ON EXCITATION FREQUENCY

The dependence of the lift coefficient on the excitation frequency is shown in figure 7.1.3. The data presented was obtained for an angle of attack of 18°. For each of the data series shown the oscillatory momentum blowing coefficient was kept constant across the range of frequencies investigated. The lift increment is expressed as the percentage increase above the uncontrolled lift coefficient, c_{L0}, at $\alpha = 18°$ of 0.748. The smallest jet momentum considered here, 0.033%, is of the order of those investigated in the previous section, whilst the other momentums considered, 0.099% and 0.131%, are considerably larger than those examined earlier. The data was obtained at a freestream velocity of 309mm/s, which corresponds to a Reynolds number of 3.08×10^4.

Some difficulty was found in conclusively identifying a trend in the dependence of forcing frequency on the lift increment. This was due to the fact that in this narrow

range being considered, the lift increment was only a soft function of frequency, and hence the variation in the lift coefficient was minimal. On the other hand, the resolution of the force sensor (0.1N) was equivalent to $\Delta c_L/c_{L0} = 5.6\%$ for the conditions at which the data in figure 7.1.3 was collected. Due to the inadequacy of the force sensor resolution, the results obtained had a high degree of uncertainty that approached the magnitude of the variations in the lift coefficients that were being investigated.

In an attempt to minimise the uncertainty of the results many individual tests were conducted. Only tests that correlated with each other to within the uncertainty of the measurements were averaged and are presented in figure 7.1.3.

It is evident in figure 7.1.3 that dissimilar frequency responses were noted for different jet momentums. For the two greater jet momentums considered, two peaks in the lift augmentation were found, approximately centred about a non-dimensional
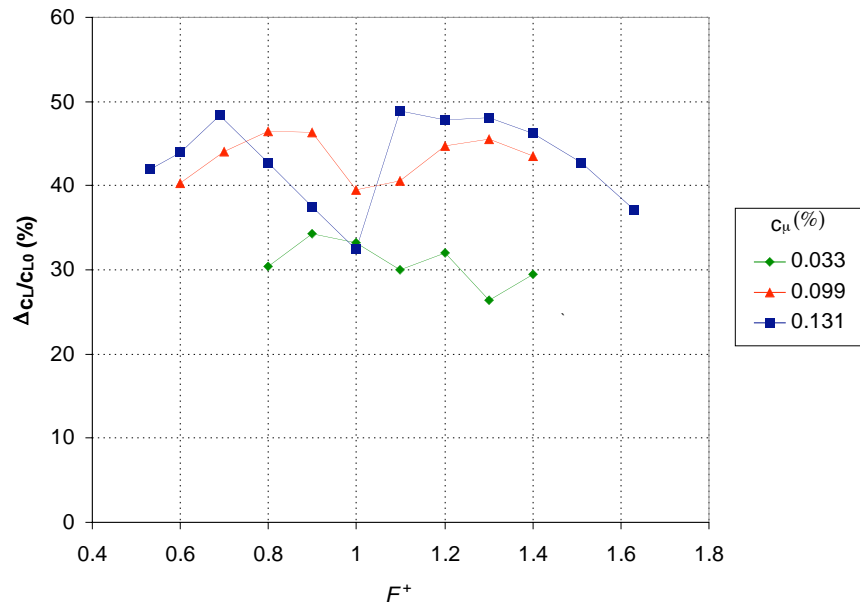

Figure 7.1.3 – Lift increment above the uncontrolled case for a range of excitation frequencies at an angle of attack of 18°.

frequency of unity, at $F^+ = 0.7\text{-}0.8$ and $F^+ = 1.3$. The absolute maximum increase of $\Delta c_L/c_{L0} = 49\%$ was found at $F^+ = 1.1$. This forcing frequency was not considered any further as an optimal forcing frequency as it did not appear as a maximum for any of the other jet momentums. Another reason why this frequency was not pursued any further was the fact that it was located next to a steep drop off in the effectiveness of the excitation. This steep drop off would be problematic if for some unknown reason the tunnel velocity or the excitation frequency were to vary slightly, altering the non-dimensional frequency such that it fell within the drop-off zone.

The cause of the reduction in the effectiveness of the jet at $F^+ = 1$ was an unexpected result. Considering the flow characterization results to follow in sections 7.3 and 7.4, no obvious hydrodynamic effect appears to result in a singularity occurring at $F^+ = 1$. Flow characterisation was not undertaken at this frequency, so it cannot be definitely concluded that the reduction in the lift coefficient was not a hydrodynamic effect.

Another potential explanation for this phenomenon was the excitation of a structural resonance frequency in the forcing system. At the upper limit of the jet

momentums attainable using the excitation system the piston cylinder arrangement was observed to deflect slightly. This deflection was clearly noticeable for jet momentums in excess of 0.2%. It is possible that at $F^+ = 1$, with the freestream velocity used, the piston-cylinder deflection occurred at a structural resonance frequency. This would result in higher relative deflections of the cylinder and hence lower volumes of fluid being displaced. It would have been possible to test this theory by varying the freestream velocity and repeating the measurements. This would have resulted in a variation of the excitation frequency for a constant non-dimensional frequency. If the drop-off in the lift augmentation was observed to have shifted to a different non-dimensional frequency then it could be concluded that the drop-off was due to a structural effect rather than a fluidic effect.

Also noted in figure 7.1.3 is a crossover in the lift increment between $F^+ = 0.8$ and $F^+ = 1$, observed for jet momentums of 0.099% and 0.131%. Behaviour of this type was not observed in the preliminary force tests, or any subsequent force tests. The magnitude of the difference between the two curves is small enough that the discrepancy falls within the experimental uncertainty, and hence it cannot be definitely concluded that such a crossover really exists.

At the lowest jet momentum considered, $c_\mu = 0.033\%$, the variation in the lift coefficient with respect to forcing frequency was much lower than for the greater jet momentums. The variation in lift increment displayed for $c_\mu = 0.033\%$ is more consistent with the findings of section 7.1.1, however it must also be noted that $c_\mu = 0.033\%$ is within the range of the momentums investigated in that section, whilst the other momentums are considerably greater.

The most effective forcing frequencies determined in this study are in the same range as those found in comparable previous experiments. For example: Seifert et al. (1996) found a peak in the lift increment at approximately $F^+ = 0.8$, but noted that a broad range of frequencies around this frequency were also effective. In further work (Seifert and Pack, 2002) the most effective forcing frequency, when determined using equation (3), was found to be $F^+ = 1.6$. In contrast to this Chang et al (1992) proposed that the most effective forcing frequencies were somewhat higher, between $F^+ = 2$ and 8.

Considering the high degree of uncertainty associated with the results in this section the only conclusions that can be arrived upon with some certainty is that at the higher jet momentums the control was most effective for non-dimensional frequencies in the range of 0.6-0.8 and 1.1-1.4. For the remainder of this investigation, promising excitation frequencies of $F^+ = 0.7$ and $F^+ = 1.3$ were pursued in greater detail.

7.1.3 DEPENDENCE ON JET MOMENTUM

For the previously identified promising forcing frequencies the variation of the lift increment with respect to jet momentum was investigated in more detail. In this part of the study the forcing frequency was held constant and the amplitude of the piston motion was varied. These experiments were conducted under similar conditions to those of the previous section: ie. a freestream velocity of 309mm/s and an angle of attack of 18°. The lift increments were normalised by the same uncontrolled lift coefficient of 0.748. As described earlier, the jet momentums investigated were limited to less than 0.2%, as above this level observable deflections of the piston/cylinder arrangement were

noted. The jet momentums were also restricted in order to avoid placing undue strain on the leading edge quadrant.

The uncertainty due to the force sensor resolution on the results in this section was the same as for the previous section: 5.6%. However, when considering the dependence of the jet momentum on the lift coefficient, much greater variation was observed. Hence, the uncertainty in the results forms a considerably smaller percentage of the magnitude of the overall trends being observed. This allows conclusions to be drawn with much greater certainty in this section when compared to the previous section.

It can be seen from figure 7.1.4 that the magnitudes of the lift increments for non-dimensional frequencies of 0.7 and 1.3 are very similar for $c_\mu < 0.15\%$. This is not an overly surprising result as the lift gains determined from figure 7.1.3 were also very similar for the two frequencies. It is noted that for $c_\mu > 0.15\%$ a non-dimensional frequency of 0.7 resulted in greater lift increments than a non-dimensional frequency of 1.3. For the reasons of excitation system deflection, the results obtained for $c_\mu > 0.15\%$ were treated with some degree of scepticism.
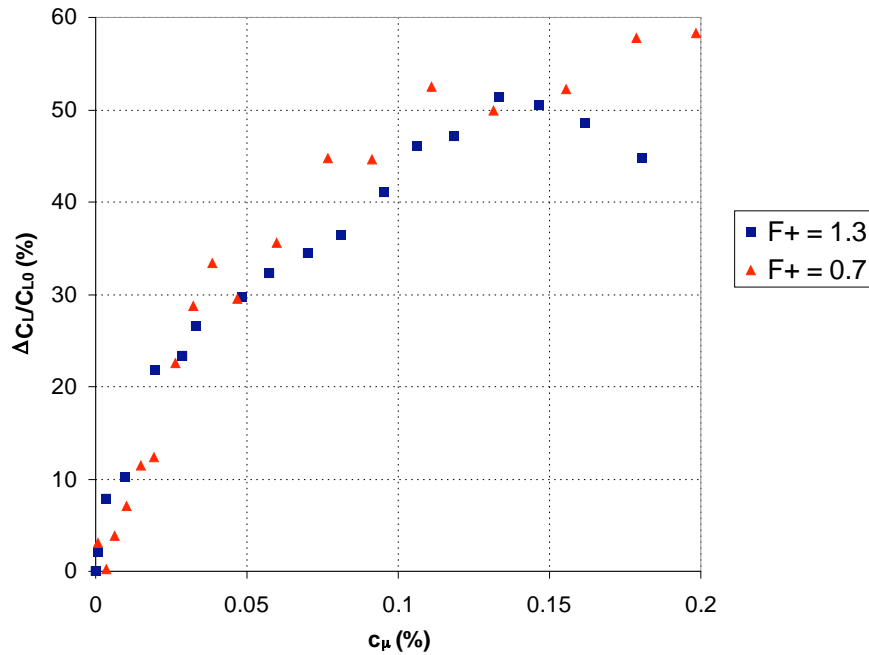
.

Figure 7.1.4 – Variation of lift increment with respect to jet momentum

A peak in the lift increment situated at $c_\mu = 0.13\%$ ($VR = 0.65$) was found for F^+ = 1.3. No such maximum was found for the lesser frequency. The magnitude of the peak was such however that once the uncertainty in the measurements was considered it was possible that the peak did not exist, and that a plateau effect was occurring. Nonetheless, at the maximum for this frequency a lift increment of 51% above the uncontrolled lift coefficient was achieved. This compares with the maximum lift increment, achieved with the greatest jet momentum considered, of 58% for the lower excitation frequency of $F^+ = 0.7$.

Assuming that the peak demonstrated exists in reality and is not an artefact of the measurement uncertainty, the physical reason for the existence of such a peak can be

explained as follows: at a momentum blowing coefficient of 0.13% the maximum reattachment effect is found from the ZNMF jet. Above this jet momentum the velocity of the ZNMF jet may be large enough to force the boundary layer to separate locally, resulting in the loss of lift demonstrated in figure 7.1.4.

A similar peak in the lift coefficient increase was found by Seifert et al. (1996), however the peak was found to be located at $c_\mu = 0.05\%$ rather than at $c_\mu = 0.13\%$ as determined here. This discrepancy is most likely attributed to differences in the geometries of the slots used for excitation. Other researchers, for example Chang et al. (1992) have suggested that a threshold amplitude exists below which excitation has little effect. Such a threshold amplitude was not observed in any of the results in this study. The numerical simulations of Donovan et al (1998) imply that no further increases in lift are gained for $c_\mu > 0.03\%$, an effect clearly not demonstrated by this investigation.

Both of the curves shown in figure 7.1.4 appear to exhibit a lift coefficient increment that is proportional to the square root of the jet momentum. This implies that the lift increment is linearly proportional to the jet velocity. This proposition was examined in more detail by plotting the dependence of the lift increment on the velocity ratio, as shown in figure 7.1.5.
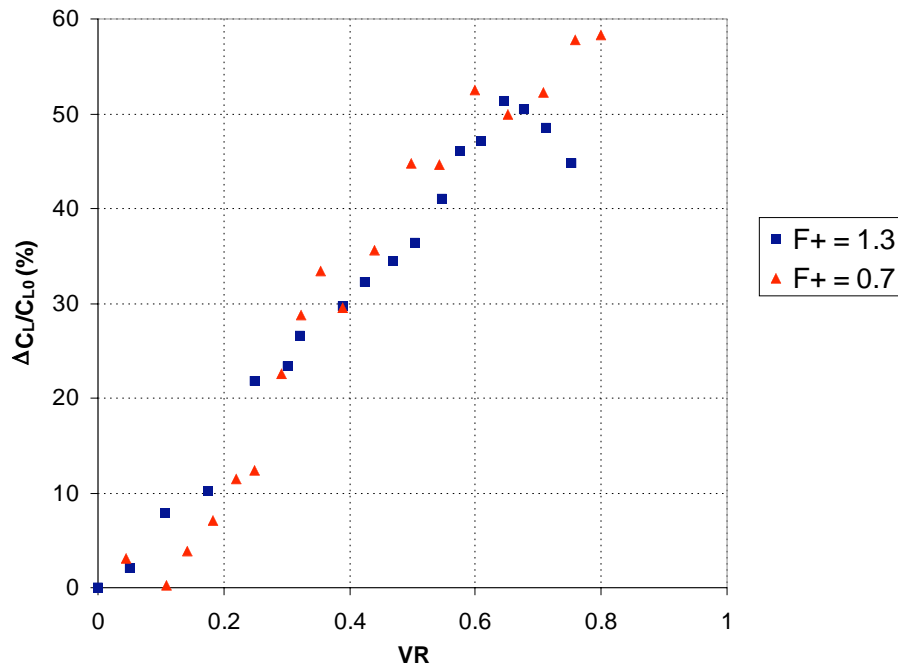

Figure 7.1.5 – Variation in lift increment with respect to jet velocity.

The dependence shown in figure 7.1.5 indicates that an approximately linear correlation between the lift increment and the jet velocity ratio does exist. This linear relationship is evident for $F^+ = 1.3$ and $c_\mu < 0.13\%$. A similar linear relationship, however displaying a steeper gradient and a negative virtual origin, is demonstrated for $F^+ = 0.7$.

7.1.4 THE OPTIMUM CONTROLLED CASE

Compilation of the results of the previous two sections revealed that the optimum parameters for maximising the post-stall lift were forcing frequencies of $F^+ = 0.7$ or 1.3, coupled with high forcing amplitudes. The forcing amplitude used for the remainder of the investigation was an oscillatory momentum blowing coefficient of 0.138%.

Figure 7.1.6 highlights the difference between the controlled and the uncontrolled lift curves. The curves were all generated at a Reynolds number of 3.08 x 10^4. In order to account for the effects of any hysteresis, the lift force was measured for both ascending and descending angles of attack. The entire measurement loop (ascending and descending) was repeated and the results averaged in order to minimise the uncertainty of the measurement.

Up to an angle of attack of 9° the controlled and the uncontrolled lift curves are almost identical, however beyond $\alpha = 9^o$ significant divergence is noted. At $\alpha = 10^o$ the uncontrolled airfoil stalls and the lift coefficient begins to diminish, eventually settling on a lift coefficient of around $c_L = 0.82$ in the deep-stall region. The controlled lift curves continue to rise unabated however, with a maximum lift coefficient of 1.17 being achieved at a stall angle of 17.2^o for $F^+ = 1.3$. This corresponds to a lift coefficient increase of $\Delta c_L = 0.368$, or 46% above the uncontrolled lift coefficient for the same angle of attack. The maximum lift coefficient produced by the controlled airfoil is 30% greater than the maximum lift coefficient of the uncontrolled airfoil. Throughout the post-stall region investigated, the controlled airfoils delivered substantial lift increments over the uncontrolled airfoil. As the angle of attack is increased beyond 20° the magnitude of the lift increment subsides. This suggests that the control mechanism is not strong enough to promote full reattachment of the flow at the higher pressure gradients found for angles of attack greater than 20°.
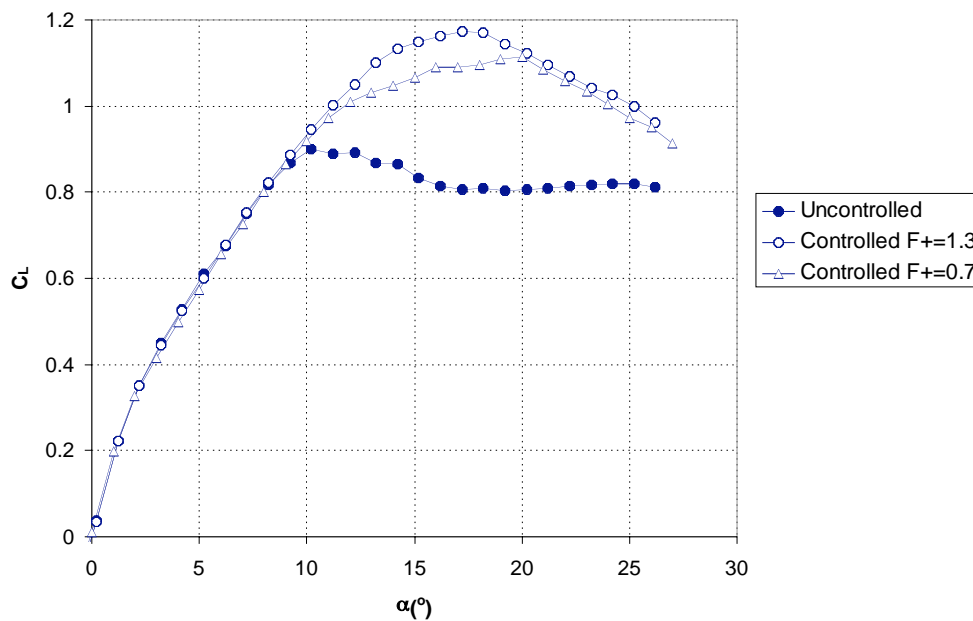

Figure 7.1.6 – Comparison of the controlled and uncontrolled airfoil lift coefficients. For both controlled cases $c_\mu = 0.138\%$

The lift increment attained using the non-dimensional forcing frequency of 1.3 was comparable to what was expected considering the results of previous sections. On the other hand, the lift increment achieved for $F^+ = 0.7$ was lower than was expected at $\alpha = 18°$. Considering the discontinuity in the gradient of the lift curve that is apparent for the $F^+ = 0.7$ case at $\alpha = 20°$, it appears as if the total possible lift increment between angles of attack of 13° and 19° was not realised. The reason for this was not able to be explained, however it suggests that implementation of the active control at a non-dimensional frequency of 0.7 is volatile, and could possibly be detrimentally affected by external factors. The relative instability of operating at $F^+ = 0.7$ was further demonstrated when the Reynolds number was reduced to 1.54×10^4. At this reduced Reynolds number similar lift increments were observed for the $F^+ = 1.3$ case, however the lift increments for $F^+ = 0.7$ were substantially reduced below those attained at $Re = 3.08 \times 10^4$. Due to the greater apparent stability of operating at a non-dimensional frequency of 1.3, the flow characterisation was predominantly carried out at this frequency.

The lift gain at 22° angle of attack found in this experiment, $\Delta c_L = 0.25$, was exactly the same as the lift gain determined by Donovan et al (1998) in their numerical simulations. Greater lift gains above the uncontrolled post-stall values were found by Chang et al (1992), however when their lift gains are considered relative to the maximum lift produced by the airfoil, the gains are substantially lower. This is due primarily to the fact that their uncontrolled airfoil exhibited a more severe stalling characteristic, resulting in larger lift reductions in the deep-stall region.

Wu et al (1998) noted that the effectiveness of separation control decreased as the angle of attack approached the uncontrolled stall angle. In their simulations the lift enhancements found at 25° were significantly greater than those determined for an angle of attack of 18°. They used the argument that 'the shear layer must be free enough to undergo the local instability' to explain this phenomenon. This finding is in stark contrast to the results presented here, where maximum lift gains were found much closer to the uncontrolled stall angle. Using the lift curve presented in figure 7.1.6 and the flow visualisations of section 7.3, it can be argued that the shear layer does not require a certain degree of freedom for the control to be effective, and that the mechanism through which the control works in fact further decreases the freedom of the shear layer.

In addition to the lift curves, the controlled ($F^+ = 1.3$, $c_\mu = 0.138\%$) and uncontrolled airfoil drag polars were also investigated and appear in figure 7.1.7. This figure presents coefficients determined for angles of attack greater than 8° only, as for angles of attack less than this the drag forces dropped to levels unresolvable by the force sensor. The resolution of the force sensor for this flow configuration was Δc_L, $\Delta c_D = 0.042$.
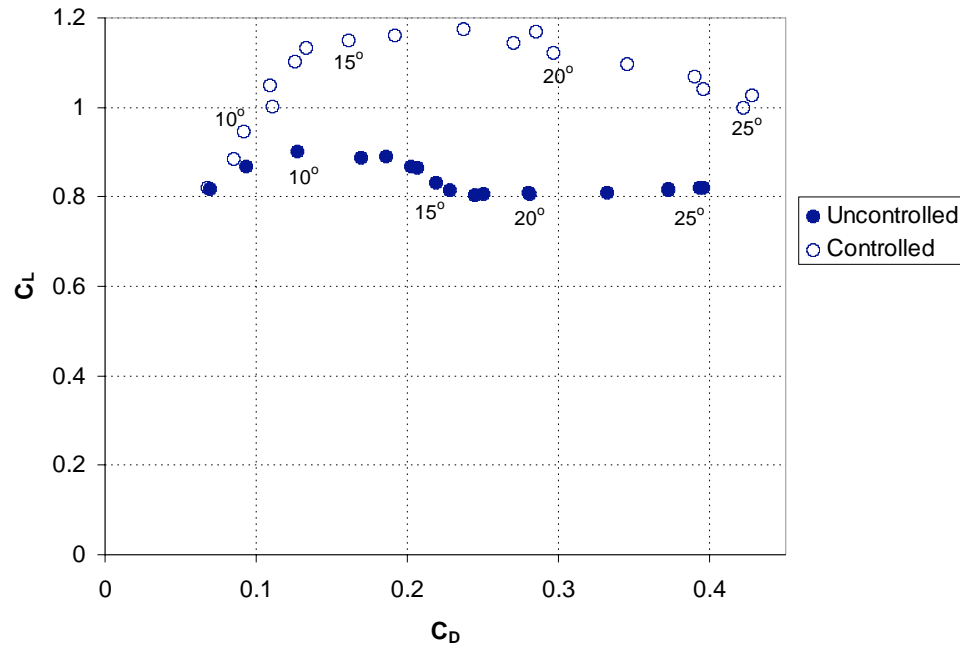
Figure 7.1.7 – Comparison of controlled ($F^+ = 1.3$, $c_\mu = 0.138\%$) and uncontrolled airfoil drag polars

The lift-to-drag ratio of the controlled airfoil remains significantly greater throughout the range of angles of attack investigated. The largest difference in drag force is found between angles of attack of 10° and 18°, where the uncontrolled airfoil has stalled and the controlled airfoil flow remains predominantly attached. This region also corresponds to the greatest increase in the airfoil lift-to-drag ratio. As the angle of attack is increased beyond 18° the drag force experienced by the controlled airfoil tends towards that experienced by the uncontrolled airfoil.

As the control mechanism employed relies on periodic excitation, it was suspected that activation of the control would result in some degree of fluctuation in the lift and drag forces acting on the airfoil. This hypothesis was tested by considering the standard error of the lift forces measured for both the controlled and the uncontrolled airfoils. This comparison appears in figure 7.1.8, where the flow conditions were the same as those used to determine the lift and drag forces in figures 7.1.6 and 7.1.7.
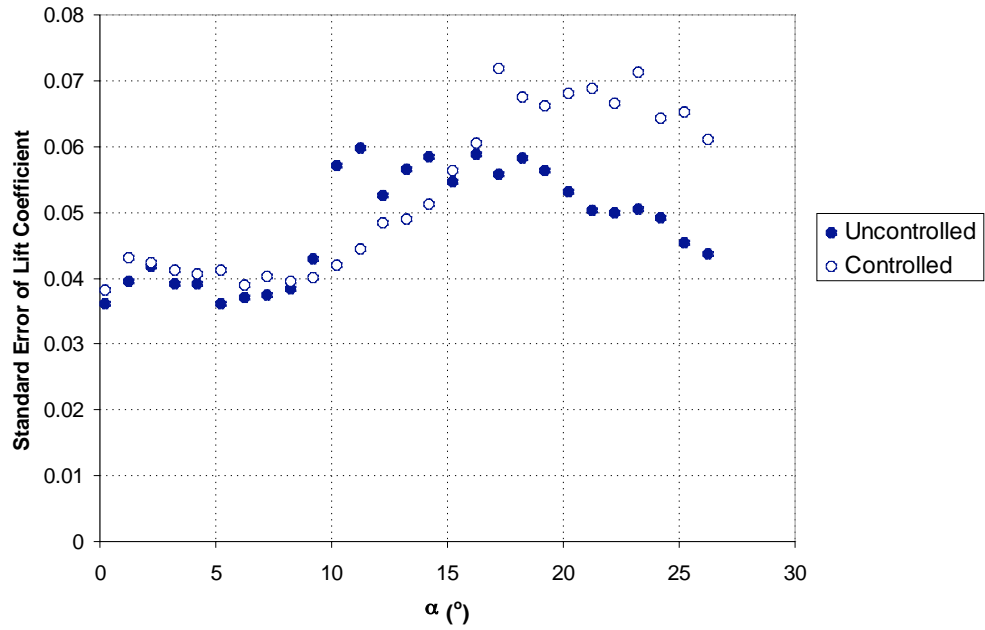
Figure 7.1.8 – Comparison of the standard error of the measured lift force for the uncontrolled and the controlled ($F^+ = 1.3$, $c_\mu = 0.138\%$) airfoils.

It can be seen that for angles of attack less than the uncontrolled airfoil stall angle the fluctuations in the measured lift force were extremely similar for both the controlled and the uncontrolled airfoils. For these angles it is apparent that the standard error is approximately equivalent to the precision of the force sensor for these flow conditions ($\Delta c_L = 0.042$). Once the uncontrolled airfoil stalled, the magnitude of the measured lift fluctuations increased dramatically. This is an expected result as once stall is reached, vortex shedding occurs from the leading edge. The time varying vortex shedding results in lift fluctuations, which would contribute to the increased standard error in the measured lift force noted in figure 7.1.8. For angles of attack between 10° and 18°, where the controlled airfoil appears to exhibit a higher degree of attachment than the uncontrolled airfoil, the measured lift fluctuations for the controlled airfoil are of lesser magnitude than for the uncontrolled airfoil. In the deep-stall region, where both the controlled and the uncontrolled airfoils have stalled, the magnitude of the lift fluctuations for the controlled airfoil increases to levels significantly greater than those observed for the uncontrolled airfoil. In this region the lift fluctuations are significantly higher for the controlled airfoil as the periodic shedding of large-scale vortices (see sections 7.3 and 7.4) results in large oscillations of the lift force.

The standard error of the force measurements gives a good indication of the magnitude of the lift fluctuations, however it is impossible to determine the real magnitude of the lift fluctuations using just the measured lift forces. This is due to the fact that the measured lift forces contain fluctuations due to fluidic effects and noise attributable to the force transducer. The two sources of fluctuations cannot be separated, and hence only their combined effect can be measured using the force sensor.

A sample time history of the measured lift force was extracted in order to quantify the effects that the low resolution of the force sensor had on the experimental results. Figure 7.1.9 shows a portion of the time history of data collected for an angle of attack of 18° with the control applied at $F^+ = 1.3$. The inadequate resolution of the force sensor is evident in the figure, which shows that the force sensor was not able to

capture the lift fluctuations accurately, however the mean of the measured forces does not appear to have been adversely affected by the low resolution to any great extent.

The data spread of the force measurements for the controlled ($F^+ = 1.3$) and the uncontrolled airfoils appear in figure 7.1.10 for $\alpha = 7°$, 18° and 25°. It can be seen that all of the force measurements are approximately normally distributed about the mean. This demonstrates that the standard deviation (standard error) of the recordings is an accurate measurement of the statistical distribution. Also apparent in the three plots is the variation of the magnitude of the measured fluctuations. It is seen that for $\alpha = 7°$ the measured lift forces for the controlled and the uncontrolled airfoils demonstrate an approximately equivalent distribution about the mean. At $\alpha = 18°$ the deviation from the mean for the controlled airfoil is smaller than that demonstrated for the uncontrolled airfoil. At $\alpha = 25°$, despite the magnitude of the standard error being greater, the relative percentage deviation from the mean for the controlled airfoil is approximately the same as that for the equivalent uncontrolled airfoil. This occurs by virtue of the greater mean lift coefficient for the controlled airfoil at this angle of attack.
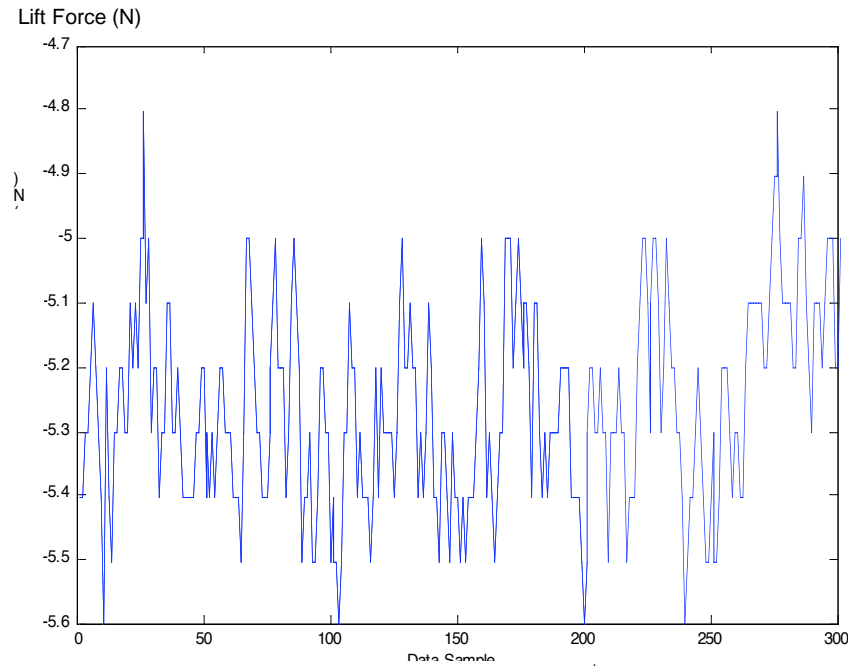

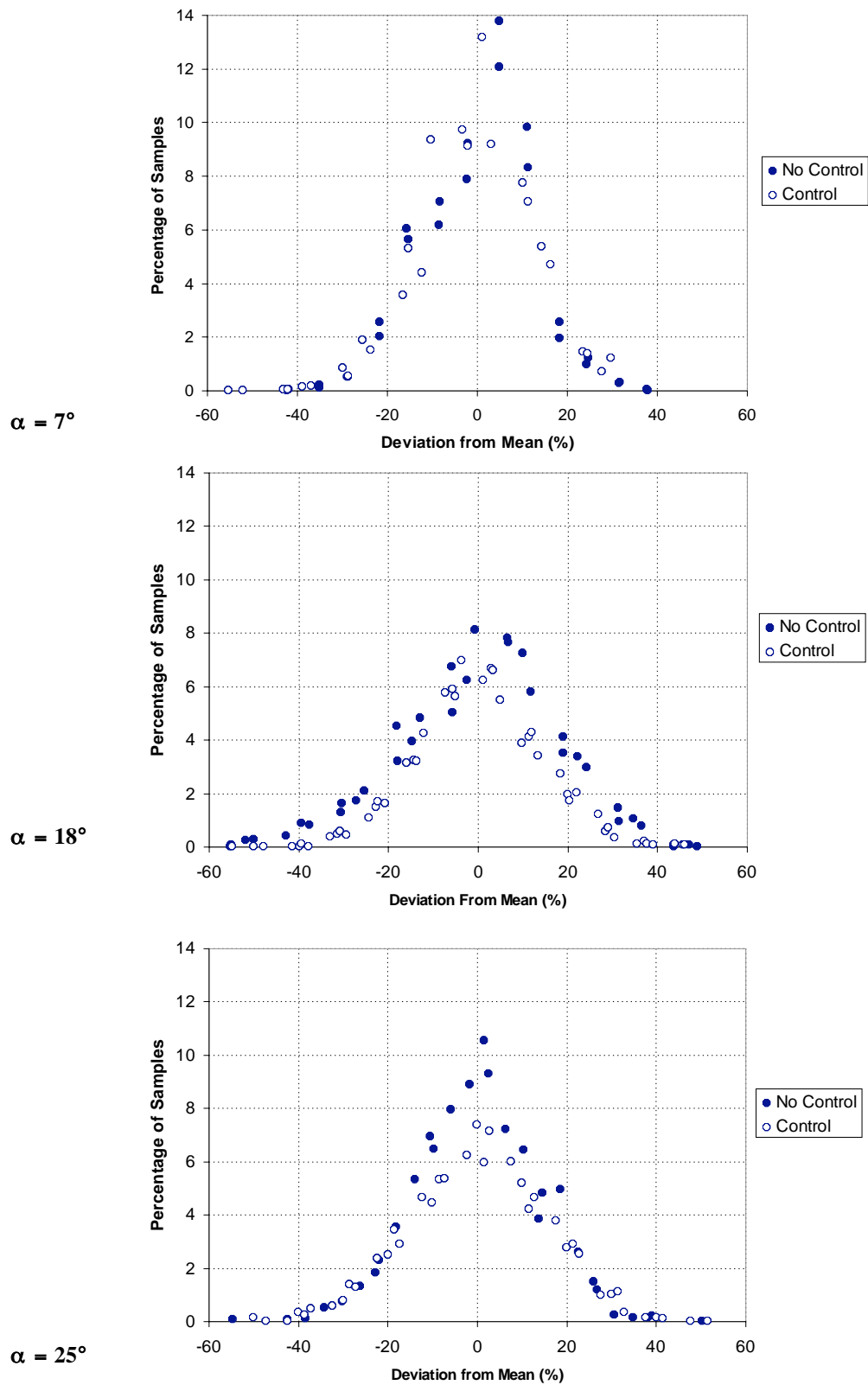**Figure 7.1.9 – Time history of the controlled airfoil (F^+ = 1.3) lift force at α = 18°.**

α = 7°

α = 18°

α = 25°

Figure 7.1.10 – Deviation of the measured lift forces from the mean, α = 7°, 18° and 25°

7.2 DYE STREAK FLOW VISUALISATIONS

The force measurement results presented in section 7.1 demonstrated that activation of the ZNMF jet resulted in greater lift and less drag being produced for angles of attack greater than 10°. This suggests that a more attached flow regime is present for the controlled airfoil in these post-stall angles of attack. This hypothesis was examined in more detail by conducting dye streak flow visualisations. The flow visualisations, and all of the other flow characterisations were conducted at $\alpha = 18°$. This angle was used as it represented the maximum divergence of the controlled airfoil lift coefficient from the uncontrolled airfoil lift coefficient. Hence, the greatest fluid dynamic effect due to activation of the jet was expected at this angle. However, it must also be noted that this condition corresponds to the point where the excitation is on the verge of losing effectiveness in controlling the flow field. Figure 7.2.1 shows the dye streak visualisations for the uncontrolled and controlled airfoils at Re = 1.54 x 10^4.
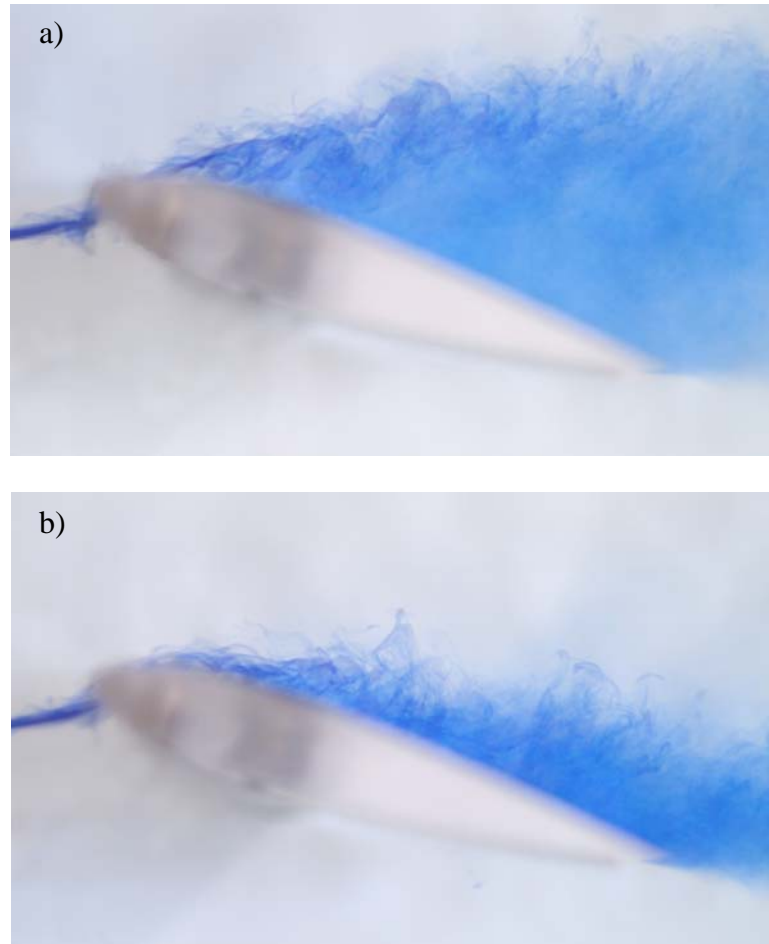

Figure 7.2.1 a) uncontrolled and b) controlled (F^+=1.3, c$_\mu$=0.13%) dye streak flow visualisations.

Figure 7.2.1 a) shows that the boundary layer of the uncontrolled airfoil has separated right at the leading edge to form a clearly defined separated shear layer. This shear layer is unable to overcome the adverse pressure gradient required for reattachment to occur. Consequently, a large region of separated flow is formed. The region of the image containing high concentrations of blue dye corresponds to this wake region. Higher concentrations of dye are present in the wake region, as a mean recirculation exists in the wake. This mean recirculation prevents the dye from

escaping, resulting in the higher dye concentrations observed. Using the blue dye as a measure of the wake region, the cross-stream size of the wake region is 60% of the chord length for the uncontrolled airfoil.

Conversely, it is evident from figure 7.2.1 b) that the flow remains attached to the airfoil for a much greater proportion of the chord length in the controlled case. As a result of this prolonged attachment, the size of the wake region that is formed is only 26% of the chord length, a 57% decrease in wake size when compared to the uncontrolled case.

The presence of the dye tube 77 mm upstream of the leading edge of the airfoil undoubtedly has some effect on the airfoil flow field. Although mounting the tube within a streamlined section minimised the effects of vortex shedding, the section still presents a significant impediment on the flow. As a result, turbulent instabilities due to the impediment interact with the airfoil flow. The magnitude and consequences of these interactions could not be quantified, however the magnitudes of the instabilities would have been equivalent for both the uncontrolled and controlled cases. Hence, it can be concluded that the change noted was due to activation of the control, and that the control was still effective despite the presence of instabilities in the oncoming flow.

7.3 PLANAR LASER INDUCED FLUORESCENCE

The PLIF images presented in this section were all generated by the addition of Kiton Red 620 fluorescent dye into the ZNMF jet cavity. For the uncontrolled case this dye was driven out of the jet orifice by the pressure head generated due to the elevated position of the dye supply bottle. For the controlled cases the fluorescent dye mixed with the fluid within the ZNMF jet cavity and was exuded into the external flow during the piston's forcing stroke. All of the controlled cases presented in this section used the predefined optimal forcing conditions of $F^+ = 1.3$ and $c_\mu = 0.13\%$.

Figure 7.3.1 reemphasises the dye streak flow visualisations of figure 7.2.1 for the same forcing conditions and angle of attack. Both of the images displayed are averaged from 64 instantaneous images. For the uncontrolled case, the trajectory of the separated shear layer is clearly evident. The presence of a massive separated region is inferred from the shear layer trajectory. In contrast, the controlled case demonstrates that the flow appears to remain predominantly attached to the upper surface of the airfoil.

The mechanism prompting the apparent reattachment of the flow was investigated in more detail by examining phase averaged realisations of the controlled flow field. These images are presented in figure 7.3.2. 8 phases were considered, where all phases were evenly spaced 45° apart throughout the excitation period. Once again, each of the images presented is the average of 64 individual images. 0° phase corresponds to the point during the excitation cycle where the piston is at bottom dead centre, and the expulsion of fluid from the leading edge slot is about to begin. Maximum jet exit velocity is reached at a phase of 90° and the expulsion of fluid is completed by a phase of 180°. A phase of 270° corresponds to the maximum jet entrainment velocity and at a phase of 360° the cycle recommences.

The generation of large vortical structures that convect downstream from the leading edge along the airfoil surface is apparent in figure 7.3.2. The development of these structures is first seen at a phase angle of 135°. At this angle, nearing the completion of the forcing stroke, the structure is observed at a location of approximately $x = 10\%c$. By the time the excitation cycle responsible for the formation of the structure has finished, the centre of the structure is observed to be located at approximately $x = 45\%c$. It is not until three quarters of the following cycle has been completed that the structure reaches the trailing edge of the airfoil. The fact that almost two complete excitation periods are required for the vortex to convect from the leading to the trailing edges translates to the presence of two vortices over the upper surface of the airfoil at any instant in time, except perhaps for a brief period of approximately 45° phase near the end of the excitation cycle.

Throughout its procession along the upper surface of the airfoil, the vortex remains in close proximity to the surface. This indicates that the local convective velocity is approximately tangential to the surface, a stark contrast to the separated shear layer trajectory depicted for the uncontrolled case. This is further confirmation of a more attached flow field.

From a phase angle of 180° onwards the vortex created precedes the bulk of the fluid ejected from the orifice. Examination of the vortex in figure 7.3.2, most notably at a phase of 270°, reveals that the vortex is of the same sign as the lifting vortex. This observation is reaffirmed in the instantaneous visualisations of figure 7.3.4 and quantified during the PIV analysis. Being of the same sign as the lifting vortex, the vortex is able to 'roll' over the surface of the airfoil. It is postulated that this rolling

motion is what allows the vortex move away from the leading edge at a faster rate than the bulk of the fluid ejected from the orifice.
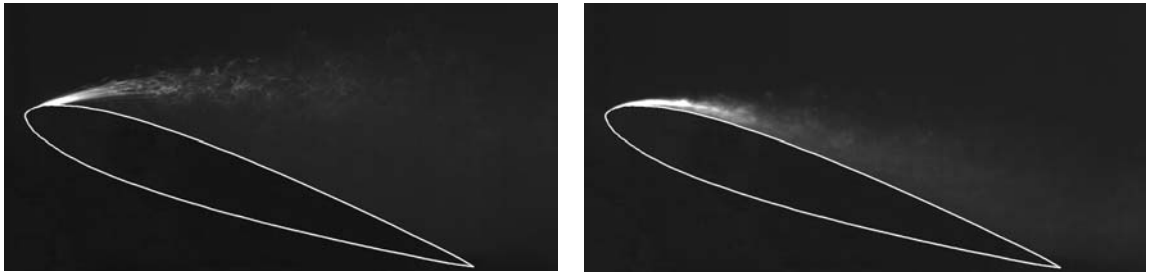

Figure 7.3.1 - Averaged visualisation of the uncontrolled (left) and controlled (right), F^+ = 1.3, c_μ = 0.13%, airfoils at α = 18°.
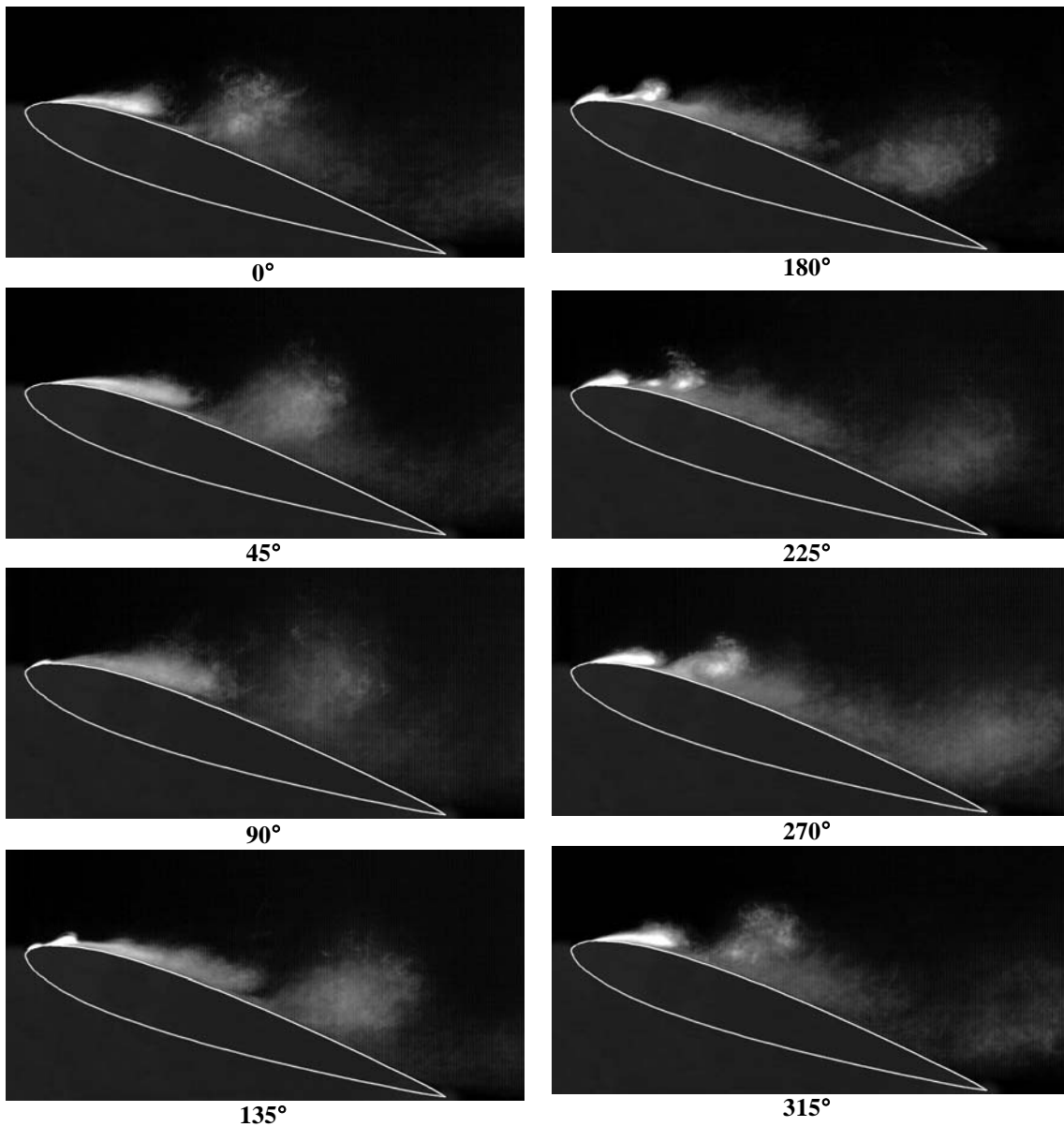

0°

180°

45°

225°

90°

270°

135°

315°

Figure 7.3.2 – Phase averaged visualisations of the controlled airfoil (F^+=1.3, c_μ=0.13%) at α = 18°.

The distance between this leading vortex and the bulk of the ejected fluid in figure 7.3.2 may in fact appear to be greater than it really is. Due to mixing with the external fluid, the dye being ejected from the leading edge slot will not faithfully remain solely with the ejected fluid. Rather, it will act as a tracer for the ejected fluid's current location, as well as the integrated regions that it has previously passed through. This mixing is what is responsible for the illusion that the vortex is accelerating away from the bulk of the fluid ejected from the leading edge slot at a rate faster than it actually is.

At a phase angle of 180° it is seen in figure 7.3.2 that the vortex responsible for the apparent reattachment of the flow originates from the near wall region. This is distinct from a vortex originating from the boundary between the fluid ejected from the leading edge slot and the freestream fluid. Had the vortex been generated from this boundary it could be postulated that the requirement for the generation of such a vortex is the periodic introduction of low speed fluid adjacent to the airfoil surface. However, as the vortex originates from the near wall region, this generation mechanism can be ruled out. Two other possible generation mechanisms exist. One of these mechanisms is the boundary layer between the ejected fluid and the airfoil surface; whilst the other is that the vortex observed is one half of the vortex pair created by the planar ZNMF jet. The first of these mechanisms can also be ruled out on the basis that the fluid ejected from the jet orifice is moving comparatively slowly relative to the airfoil. The generation of such large-scale vortices is never realized when the airfoil is subjected to the freestream flow velocity, and hence large-scale vortices would not be generated when the relative velocity between the fluid and the boundary was even lower. Hence, the only mechanism that could be responsible for the generation of the structures observed is the vortex pair formed by flow separation at the ZNMF jet orifice.

Further understanding of the physical mechanisms responsible for the alteration of the global flow field can be gained from examining instantaneous visualisations. Figure 7.3.3 depicts an instantaneous snapshot of the uncontrolled airfoil, whilst in figure 7.3.4 snapshots at a series of discreet phase angles for the controlled airfoil are presented.
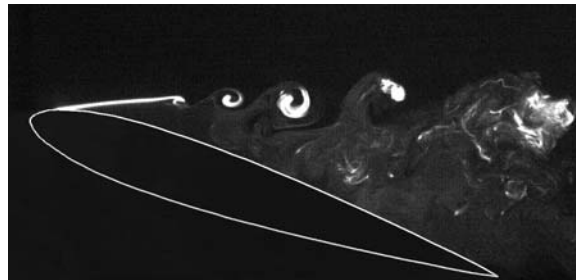

Figure 7.3.3 – Instantaneous visualisation of the uncontrolled airfoil at $\alpha = 18°$.

The instantaneous snapshot of the separated shear layer in figure 7.3.3 reveals the regular, periodic shedding of vortices from the leading edge that occurs for the uncontrolled case. Initially the separated shear layer is laminar and continuous. This continuous shear layer soon rolls up to form a train of initially laminar vortices. As these vortices progress they are seen to undergo transition to turbulence before they reach a position level with the trailing edge.

Nearer to the leading edge the separated shear layer is dominated by high frequency vortex shedding. Towards the trailing edge however it can be seen that the scale of the structures appears to have grown significantly. This is due partially to the interaction of the leading edge separated shear layer with the larger-scale trailing edge vortices. The superposition of higher and lower frequency structures: the higher

frequency leading edge vortices and the lower frequency trailing edge vortices, contributes to the apparently random nature of the separated region.

A series of 164 realisations of the uncontrolled case were collected at a frame rate of 10 frames per second. By manually counting the number of vortices shed the average leading edge shedding frequency for $\alpha = 18°$ and $U_\infty = 150$ mm/s was determined to be approximately 5.5 Hz. This corresponds to a Strouhal number based on the chord length of $St = 3.66$. Comparing the ratio of the optimum forcing frequencies, f, with the natural shedding frequency, f_{shed}, we find the following ratios:

$$\text{for } F^+ = 0.7: \quad \frac{f}{f_{shed}} = \frac{1}{5.2} \qquad\qquad \text{for } F^+ = 1.3: \quad \frac{f}{f_{shed}} = \frac{1}{2.8}.$$

It is noted from the two ratios that the lower effective forcing frequency is close to the 4th sub-harmonic of the natural shedding frequency, whilst the upper effective forcing frequency falls close to the 2nd sub-harmonic of the natural shedding frequency. Considering the approximate nature with which the natural shedding frequency was determined, and the uncertainty involved in determining the optimal forcing frequencies, it is quite possible that the most beneficial forcing frequencies lie at the 2nd and 4th sub-harmonics of the natural leading edge shedding frequency. In order to confirm this hypothesis more accurate measurements of the natural shedding frequency are required. Confirmation of the hypothesis also relies on the force measurements and the determination of the leading edge shedding frequency being carried out at the same Reynolds number, something that was not done in this case. Another point to be considered is the fact that the natural shedding frequency of the airfoil is likely to be a function of angle of attack as well.

Extending this hypothesis to comparisons with the measurement of the lift increment for different forcing frequencies, a potential explanation for the reduction in the lift increment noted around $F^+ = 1$ can be arrived upon. Given that reduced effectiveness of the control was noted around $F^+ = 1$, and around $F^+ = 1.8$, and that these frequencies lye close to the 1st and 3rd sub-harmonics of the natural shedding frequency, it could be postulated that forcing must occur at an even sub-harmonic of the natural shedding frequency in order for maximum effectiveness. Once again, it must be noted that the hypotheses presented here are based on some very approximate measurements and require further research before they can be confirmed.

The above hypotheses assume that the effectiveness of the control is determined by the excitation frequency's relationship with the uncontrolled leading edge shedding frequency. Alternatively, and perhaps more likely, is that the most effective forcing frequencies are determined by the residence times of the vortices over the upper surface of the airfoil. Too slow an excitation frequency would lead to periods between the formation of vortices where the airfoil is effectively uncontrolled, whilst too high an excitation frequency may lead to vortices whose size is too small to affect significant control on the flow field. If it is assumed that the vortex residence time is the dominant parameter in determining the effectiveness of the control then a more meaningful definition of the non-dimensional excitation frequency could be proposed using the actual vortex residence period normalised by the vortex residence period required for exactly one vortex to be present over the upper surface of the airfoil at all times.

Figure 7.3.4 depicts instantaneous visualisations of the airfoil undergoing excitation at $F^+ = 1.3$. At a phase angle of 180° the presence of a number of smaller vortices around $x = 20\%c$ is evident. Examining all of the realisations available of the flow it was noted that anywhere between 2 and 5 vortices were discernable at this phase angle. Between a phase angle of 180° and 270° the multiple smaller vortices have

coalesced to form a larger, more intense vortex. By virtue of its greater size, the core of the single spanwise structure is offset a significant distance further away from the surface than the multiple, smaller vortices. This single vortex proceeds to convect along the remaining 60% of the airfoil surface. It is speculated that a vortex pairing, or a series of vortex pairing events, is occurring between a phase angle of 180° and 270°. These pairing events promote the transition of the multiple smaller vortices to a larger more intense structure. Note that in the realisations presented in figure 7.3.4 the vortex from the previous excitation period is not immediately obvious, however is present over the latter half of the chord.
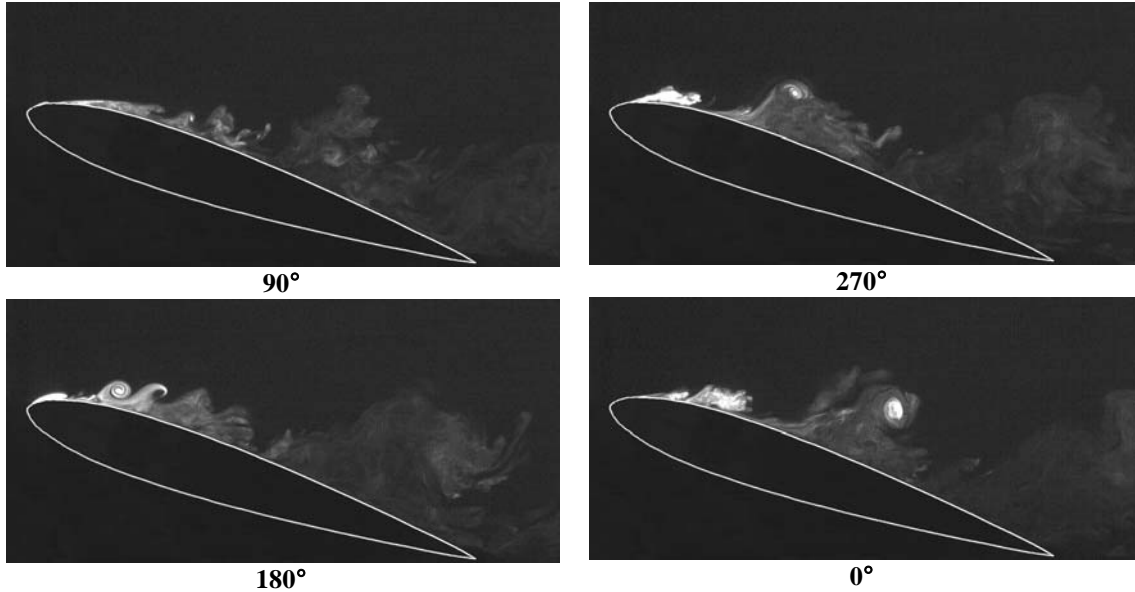

| 90° | 270° |

| 180° | 0° |

Figure 7.3.4 – Instantaneous visualisations of the controlled airfoil (F^+=1.3, c_μ=0.13%) at α = 18°.

It was observed earlier, however is more apparent in figure 7.3.4 that the vortices over the upper surface of the airfoil are always of a negative sign. It was also noted earlier that a vortex pair is created when flow separates at the sharp edges of the orifice of a planar, 2-D, ZMNF jet. The question that hence remains is: what has happened to the other half of the vortex pair? The answer to this is likely to be that the positive half of the vortex pair is annihilated by superposition of vortices of negative sign, which are inherent in the boundary and shear layers for this flow configuration. Whilst the inherent negative vorticity of the unforced flow forms a hostile environment for the positive vortex, it creates a favourable environment for the amplification of the negative sign vortex created by the ZNMF jet. This in turn results in the negative sign vortex growing in magnitude and strength to the point where it is able to affect the global flow field dynamics.

Up until this point all of the flow visualisations presented have been conducted at the upper effective forcing frequency, F^+ = 1.3. As a comparison, flow visualisations were conducted at the lower effective frequency, F^+ = 0.7, with an identical jet momentum of c_μ = 0.13%. As was noted in section 7.1.4 lift increments that were greater than those obtainable with a forcing frequency of F^+ = 1.3 were realisable with F^+ = 0.7. However, it was also noted that at a reduced Reynolds number of 1.54×10^4 the same lift coefficient increments were not obtainable. Visualisations were hence employed to investigate why this was so.
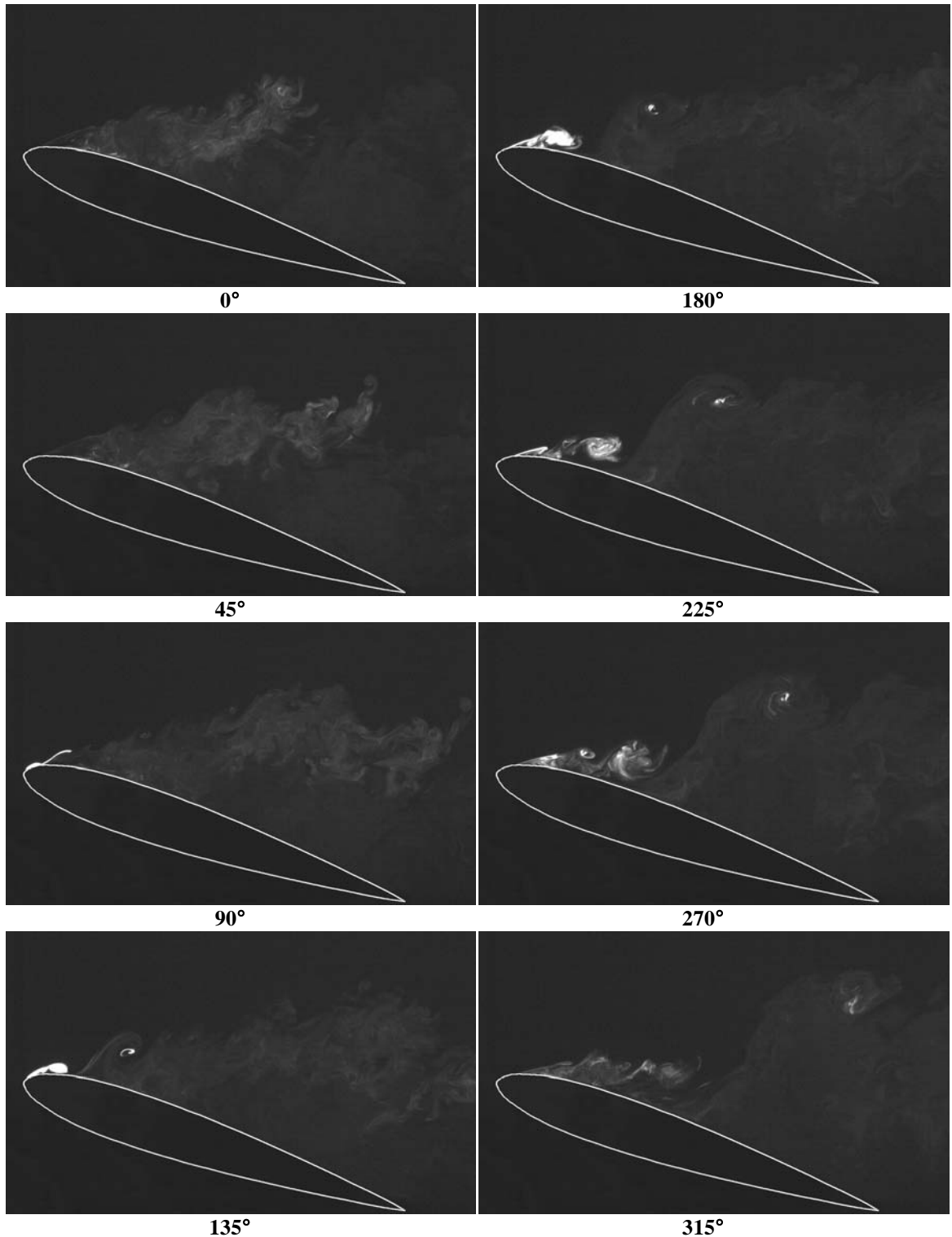
Figure 7.3.5 – Instantaneous visualisations of the controlled airfoil (F^+=0.7, c_μ=0.13%) at $\alpha = 18°$.

Figure 7.3.5 shows 8 instantaneous visualisations taken successively throughout a single forcing period at $F^+ = 0.7$. It is apparent in the figure that the control was unable to effect reattachment of the flow at this angle of attack. As such the vortices generated follow the trajectory of the separated shear layer of figure 7.3.1, rather than the attached flow demonstrated for $F^+ = 1.3$ in figure 7.3.2. As the vortices follow a trajectory that appears to be identical to the trajectory of the separated shear layer it can

be assumed that these vortices have little or no effect on the lift and drag produced by the airfoil. This can be assumed as despite the fact that the dynamics of the shear layer are being changed, the magnitude of the separation region, which is responsible for the loss of lift and increase in drag at post-stall angles of attack, remains unchanged.

Phase averaged dye visualisations of the forced case with $F^+ = 0.7$ were attempted, however the resulting images (not shown) did not show structures that were as clearly defined as those depicted for the $F^+ = 1.3$ case. Examining a history of instantaneous visualisations revealed the reason for the poor correlation between the individual realisations of the same phase angle. For some excitation cycles the vortices generated followed a trajectory similar to that shown in figure 7.3.5, however for other forcing cycles the trajectory followed was closer to the surface of the airfoil. This is an indication that at an angle of attack of 18° for these forcing conditions the leading edge shear layer was undergoing significant oscillations due to the influence of the shedding of large-scale trailing edge vortices. The sequence of images presented in figure 7.3.5 is an example of one of the forcing cycles in which the shear layer was in its most separated state. The behaviour described above suggests that this configuration was just beyond the effective limit of the applied control and that the adverse pressure gradient was too great for the excitation to counteract.

Also noted in figure 7.3.5 is the fact that for the lower effective forcing frequency, $F^+ = 0.7$, it required approximately 1 complete excitation period for the vortex generated at the leading edge to convect to a location in line with the trailing edge. For the upper effective forcing frequency, $F^+ = 1.3$, it was noted earlier that the vortex was resident over the upper surface of the airfoil for slightly less than two full excitation periods. This led to the postulation that between one and two spanwise vortices must be resident over the upper surface of the airfoil at any instant for the control to be effective. The lower limit of this proposal is somewhat intuitive, if there is a period between the generation of vortices where no vortex is present then the flow will revert back to the uncontrolled flow field. This observation is consistent with the findings of Seifert et al. (1996) who inferred from phase locked surface pressure measurements that 'no more than two eddies should reside at any instant over the previously separated region.'

Wu et al. (1998) proposed that the wake pattern of an actively controlled airfoil assumed the structure exhibited in figure 7.3.6. This is in contrast to the uncontrolled airfoil wake pattern where vortices of negative sign, shed from the leading edge, and vortices of positive sign, shed from the trailing edge, are approximately evenly spaced throughout the wake. In the proposed model of the wake region the vortices shed from the controlled airfoil are seen to form vortex couples with a large region of downward moving flow between the couples and only a small region of upward moving flow in the middle of each couple. This configuration leads to an increase in the downwash aft of the airfoil, and was used as a possible explanation for the lift increases observed when the control was activated.

Figure 7.3.6 – Controlled airfoil wake pattern proposed by Wu et al. (1998).

PLIF was used to examine the wake structure behind the controlled airfoil in an attempt to confirm the wake pattern proposed by Wu et al. (1998). This would have been done most efficiently by introducing dye from the trailing edge of the airfoil, however it was achieved with some success using the leading edge injection implemented previously. Instantaneous flow visualisations of the airfoil wake are shown in figure 7.3.7 for both $F^+ = 1.3$ and $F^+ = 0.7$.
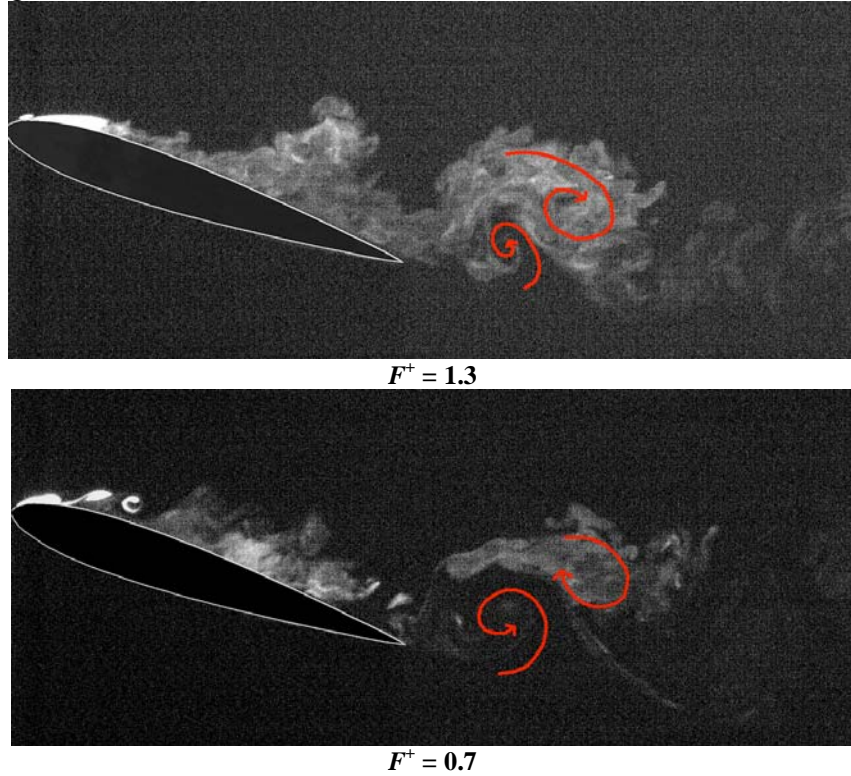

$F^+ = 1.3$

$F^+ = 0.7$

Figure 7.3.7 – Interaction of upper surface and trailing edge vortices on the controlled airfoil at α = 18°.

It is seen in figure 7.3.7 that vortex couples are formed in the airfoil wake. These vortex couples are similar in configuration to those proposed by Wu et al. (1998). It is observed that there exists significantly more space between the successive vortex couples (in both cases the previous vortex couple is far enough downstream to have escaped the field of view of the camera) than between the vortices that make up the couple. This lends weight to the increased downwash argument proposed by Wu et al. (1998).

In figure 7.3.7 the wake pattern has been displayed for two different forcing frequencies in order to show that the generation of the vortex couple is a definite effect of the forcing, rather than merely being a coincidence of the excitation being at the right frequency to promote the generation of such a couple.

It is an important realisation to make that the trailing edge shedding frequency is effectively being modulated by a control that is primarily aimed at affecting the leading edge shear layer. When considered a little more closely, it is not surprising that the trailing edge shedding frequency is being controlled as well. The introduction of periodic disturbances over the upper surface of the airfoil will produce complimentary periodic fluctuations of the local pressure. The flow around the trailing edge will naturally see these periodic fluctuations in pressure, which will effectively act as a cyclic driving force for the formation of trailing edge vortices. As such, the flow is modified so that the trailing edge vortices are shed in a periodic, controlled manner.

7.4 INTERPRETATION OF THE FLOW STRUCTURE RESPONSIBLE FOR REATTACHMENT

In the previous sections of this report significant observations have been made which yield an insight into the structure of the flow field that leads to reattachment occurring. The question of why the addition of spanwise structures leads reattachment of the flow is now tackled. The explanation offered here is the opinion of this author and is not necessarily the only possible explanation of the changes that have been observed.

Multiple mechanisms, rather than just a single mechanism, are believed to exist through which the control works. All these mechanisms directly affect the leading edge shear layer.

Significant alteration of the trajectory of the shear layer, as was observed in the experimental results, must occur close to the shear layer origin. Beyond this point the shear layer is displaced further away from the upper surface of the airfoil and hence more energy would need to be expended in order to alter the shear layer's trajectory. Therefore the vortex generated by the ZNMF jet has its greatest effect on the shear layer at its origin, which has been indicated in figure 7.4.1.
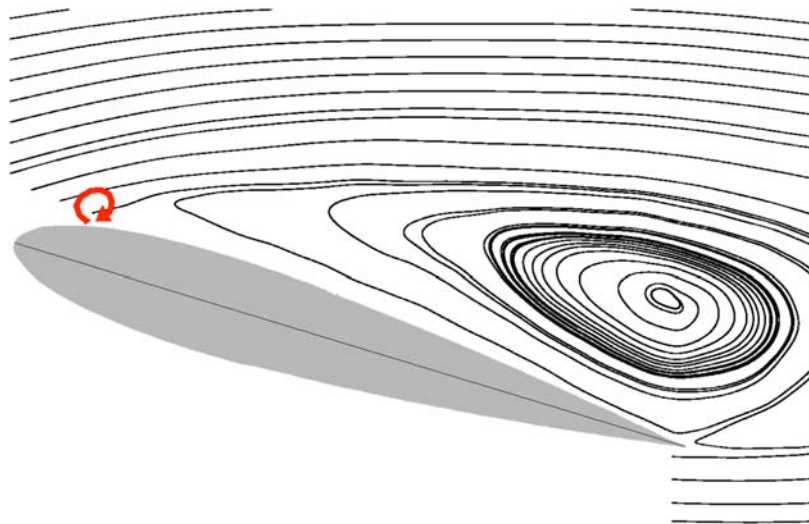

Figure 7.4.1 – The most effective location for the controlling vortex on a separated flow.

The vortex pair generated by the ZNMF jet has had sufficient residence time during its propagation from the leading edge to the separation location for two things to occur. Firstly, the positively rotating vortex is amplified by the natural shear direction of the boundary layer. It has been seen to be amplified further by the coalescence of multiple smaller instabilities. The second occurrence is that the same natural shear forces have destructively interfered with the positively rotating vortex to the point where it is effectively undetectable above the natural instabilities.

From the separation point onwards the positively rotating vortex has a high degree of influence on the separated shear layer. The addition of large-scale vorticity into a shear layer greatly increases the entrainment of the shear layer. This entrainment enhances mixing across the layer, which helps to bring high momentum fluid into the wake region. The magnitude of the velocity ratio used was such that linear instability of the shear layer was bypassed and the control immediately affected non-linear instability

of the shear layer. Furthermore, the entrainment of this lifting vortex is asymmetric; greater entrainment occurs on the upper side, where the freestream brings larger momentum into the vortex (Wu et al, 1998). This has the effect of turning the vortex downward towards the airfoil surface, aiding the reattachment process.

The fact that a strong negative vortex, rather than a positively rotating vortex or a vortex pair, is superimposed on the shear layer has further advantages. The negative rotational energy of this vortex is partially transferred to the shear layer by the fluid viscosity. This in turn further promotes the shear layer to deflect closer to the airfoil surface.

The enhanced entrainment of the shear layer and the transfer of rotational energy to the shear layer both affect significant changes on the flow field whilst the vortex exists in the forward portion of the airfoil. However, it is noted that a continuous stream of closely spaced vortices was not available. In fact, significant spacing, of the order of 50%c, existed between the vortices generated. If these vortices were to affect the shear layer at the aforementioned point and then subsequently disappear for the remainder of the excitation period, the shear layer would no doubt return to its naturally separated state during the rest of the forcing cycle. This was not however observed in any of the experimental results; hence a force must exist that promotes the boundary layer to remain attached to the surface throughout the remainder of the forcing cycle.
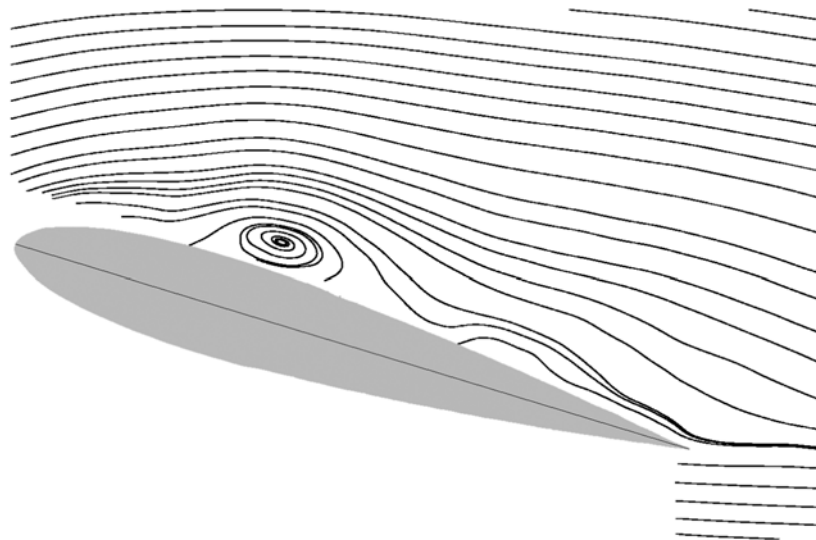

Figure 7.4.2 – Vortex location late in the forcing period.

The force promoting the flow to remain attached is apparent when the streamlines for the controlled airfoil at a phase towards the end of the forcing cycle are observed. This phase is depicted in figure 7.4.2 where it is seen that no vortex has existed near the separation point for a considerable time. The presence of the vortex downstream of the natural separation location deflects streamlines away from the surface. This deflection results in an increase in the local pressure gradient upstream of the vortex; otherwise interpreted as an alleviation of the local adverse pressure gradient. Relaxation of the adverse pressure gradient reduces the force attempting to separate the boundary layer. Hence, prolonged attachment of the boundary layer is realised.

Downstream of the vortex a greater adverse pressure is formed than would naturally exist if the vortex were not present. If the vortex were a solid body, then separation would occur on the lee side of this body. However, as the vortex is rotating

in a clockwise direction with an outer streamline velocity closely matched to the freestream velocity, no boundary layer is formed and hence separation from the lee side of the vortex is mitigated. This drags the external fluid towards the surface, minimising the effects of separation from the lee side of the vortex.

Considering the above arguments it is observed that the forcing must be of sufficiently high a frequency that the vortex does not drift too far away from the shear layer origin before the next vortex is generated. Otherwise, as the vortex drifts away from the shear layer origin the adverse pressure gradient alleviation effects will diminish and shear layer separation between the successive vortices will occur.

8.0 APPLICATIONS OF THE TECHNOLOGY

At this point it is instructive to consider the viability of the use of active flow control using a ZNMF jet on a full-scale aircraft. As the controlled flow has been parameterised using a number of non-dimensional groups, relatively simple scaling arguments can be employed to investigate the forcing conditions that would be necessary in order to apply this technology in the full-scale. For this analysis it is assumed that active control will be used as a replacement high-lift device for activation at take-off conditions. In this case the control can be seen as a replacement for a leading edge slat or a mechanism through which the size of the trailing edge flaps can be reduced. The benefit of applying active control in this situation is to indirectly reduce the induced drag acting on the aircraft by affording a weight saving in the high-lift devices.

In doing this analysis a number of assumptions need to be made. The most significant of these assumptions is that the control effectiveness will not be adversely affected by an increase of Reynolds number. This is a substantial assumption to make, however it is supported by the investigations of Seifert and Pack (2002), where it was found that the Reynolds number had a negligible effect on the flow and its control for Reynolds numbers up to 26×10^{6}.

The optimal control parameters of $F^{+} = 1.3$ and $c_{\mu} = 0.14\%$ will be applied to this situation. It will be assumed that the aircraft in question has a take-off speed of 300km/h (83.3 m/s) and the control is applied over an airfoil section with a chord length of 3m.

Using the non-dimensional group $^{h}/_{c} = 0.155\%$ the 2-D slot height for this aircraft configuration would be of the order of 4.65mm. An excitation frequency of 36 Hz would be required to achieve a non-dimensional frequency of 1.3 at take-off conditions. To achieve the necessary jet momentum, an rms jet exit velocity of 56 m/s would be required.

It is now also assumed that an embedded, sinusoidally oscillating membrane with a width of 150mm forms the ZNMF jet. In this case the contraction ratio between the membrane and the jet orifice is 32. Note that negligible losses due to the compressibility of air within the orifice are also assumed. In order to produce the necessary control with this actuation system the membrane must oscillate at 36 Hz with amplitude of 10.8mm.

In this simplistic example it is seen that producing the required pressure oscillations in a full-scale application must incorporate a challenging actuator design. Nonetheless, if the technical limitations associated with actuator design can be overcome, active flow control can offer significant benefits if it can provide less of a

weight penalty than traditional movable wing surfaces. To highlight the potential advantages of active control an energy balance between energy expended for active control and the energy saved indirectly through reduction of induced drag is presented.

If the hypothetical aircraft being considered is operating as a long-haul passenger aircraft it can be assumed that high-lift devices will only be employed for 5 minutes during take-off and landing, out of a flight that can potentially last for 10 hours. In order for active control to be an attractive option the energy expended must be less than the energy saved due to reduced drag:

$$P_{control} \, t_{hl} < P_{saved} \, t_{cruise} \qquad (13)$$

Here, $P_{control}$ is the power consumed by the active control (including all associated losses), P_{saved} is the drag power saved by decreasing the overall aircraft weight, whilst t_{hl} and t_{cruise} are the length of time which active control is applied for and the cruising time respectively. The drag power saved can be determined from the decrease in the lift required and by assuming a lift-to-drag ratio of 18 for the overall aircraft.

$$P_{saved} = \Delta D U_{cruise}$$
$$P_{saved} = \frac{\Delta mg}{L/D} U_{cruise} \qquad (14)$$

Hence, in order for a net energy saving:

$$P_{control} < \frac{t_{cruise}}{t_{hl}} \frac{\Delta mg}{L/D} U_{cruise} \qquad (15)$$

For a cruising speed of 280 m/s along with the previous assumptions, the power consumed by the active control device in order for it to be an economical option must be less than:

$$P_{control} < \frac{60 \times 10}{10} \frac{\Delta m \times 9.81}{18} \times 280 \qquad (16)$$
$$P_{control} < 9.16 kW/kg$$

Hence, it can be concluded that for the hypothetical aircraft chosen in this example it is economical from an energy balance perspective to employ active control as long as the active control consumes less than 9.16 *kW per kg* of weight saving the system offers over a conventional flap/slat system. Note that this figure could potentially be even higher, as in this simplistic example compounding weight savings due to the fact that less fuel would need to be carried have not been accounted for. Note that this example considers only an energy balance and does not account for additional factors such as safety, noise and economics. Nonetheless, it is clear that if weight savings can be realised through the application of active control as a high-lift device significant energy savings can result, even if high power consumptions are required to drive the device.

9.0 RECOMMENDATIONS FOR FURTHER RESEARCH

In this investigation active flow control using a ZNMF jet around an ideally 2-Dimensional airfoil was examined. However, the application of active flow control will most certainly exist in the control of 3-Dimensional flows. Hence, the 3-Dimensional effects of such a control device need to be examined in greater detail. This can be achieved using a similar experimental apparatus as was used in this investigation,

however with the airfoil only partially submerged within the working fluid. This would allow for a strong tip vortex to be generated, and the interaction between the controlling vortices and the tip vortices could be studied in more detail.

Different optimal jet momentums have been reported in a number of studies, all of which have used different geometries. An attempt to identify the most efficient slot height required to implement active flow control would be extremely valuable. Such a study would no doubt incorporate the identification of the relationship between the control effectiveness, the jet momentum and the jet velocity ratio. In doing so different slot heights would need to be investigated in order to decouple the jet momentum and velocity, which cannot be varied independently with a slot of fixed height.

A number of studies have incorporated an investigation of the most effective slot angle relative to the surface. To the best of this author's knowledge however, these investigations have not included a detailed study of the effect of canting the jet in the upstream direction. Most investigations have focused on cant angles in the downstream direction. However, an upstream canted jet leads to the greatest velocity gradients being formed between the jet and the freestream. Greater velocity gradients result in the formation of the strongest vortices, which suggests that an upstream configuration may be more effective than a wall-normal or downstream canted jet.

The effect of using different orifice geometries could be investigated. A 2-D slot running the entire length of a large aircraft wing presents significant structural and manufacturing difficulties. Hence it is more likely that a series of shorter slot sections would be used in place of a continuous slot. The study of the 3-Dimensional flow structure at the boundary between an actively controlled and an uncontrolled airfoil section is hence required. This study could be extended in order to determine the optimal spacing of different slot sections.

This study has focused on rectangular jet orifices only. Of course many other potential orifice shapes exist, which may or may not be more effective in controlling the flow. In altering the orifice shape to one with a lower aspect ratio, for example a circular hole, the effect of the jet will be altered significantly. This is due to the fact that a circular orifice will result in the formation of a horseshoe necklace vortex and a strong streamwise vortex, rather that the spanwise vortices noted in this study. Obviously these vortex distributions will have markedly different effects on the control of separation.

Active flow control studies may be found to be more applicable to flight scenarios if they are applied to geometries that already have a boundary layer formed on them. This can be achieved simply by modelling the upper surface of an airfoil as a backward facing ramp, and allowing the boundary layer to grow in front of the ramp before control is applied at, or just before, the ramp discontinuity.

More efficient operation of active flow control may be found if multiple ZNMF jets are employed. Many factors can be varied when multiple jets are employed. The location of the jets, both in the cross-stream and streamwise directions can be investigated. The effect of using multiple jets acting out of phase to one another is also an area that may produce promising results.

To conclude these investigations must be complemented with quantitative flow measurements using high resolution PIV to obtain more in-depth understanding of the effect and interaction of ZNMF jet with separated boundary layer flow. These types of measurements require great care and are elaborate but are essential.

10.0 CONCLUSIONS

This study has shown that a wall-normal ZNMF jet located at the leading edge of a NACA 0015 airfoil is an effective active flow control device. Significant lift increments have been noted in the post-stall region of the uncontrolled airfoil when forcing was applied with the appropriate frequency and momentum input. Optimal forcing parameters, defined as the parameters leading to the greatest increase in the maximum lift coefficient, were determined in terms of the non-dimensional forcing frequency, the oscillatory momentum blowing coefficient and the jet velocity ratio. The structure of the flow field around the optimally controlled airfoil was divulged successfully and compared to that of the uncontrolled airfoil.

A relatively broad range of effective forcing frequencies were identified, ranging from $F^+ = 0.6$ to $F^+ = 1.4$. In this range the optimal forcing frequencies were determined to be a pair of frequencies symmetrically offset from a non-dimensional frequency of unity at $F^+ = 0.7$ and $F^+ = 1.3$. The effect of varying the jet momentum was investigated at both of these frequencies. At an angle of attack of 18°, for both of the frequencies investigated, the lift coefficient increase was approximately proportional to the square root of the jet momentum, and hence linearly proportional to the jet velocity ratio. A peak was found in the effectiveness of the active control at $F^+ = 1.3$ for a momentum corresponding to $c_\mu = 0.14\%$. No such peak was determined for a frequency of $F^+ = 0.7$ in the range of jet momentums investigated.

Activation of the control with the optimal excitation parameters of $F^+ = 1.3$ and $c_\mu = 0.14\%$ resulted in the stall angle of the airfoil being mitigated from an angle of attack of 10° up to an angle of attack of 18°. Under these controlling parameters a maximum lift coefficient increase of 46% above the uncontrolled lift coefficient occurred at an angle of attack of 18°. Significant lift increments, and an increase in the lift-to-drag ratio of the airfoil were noted throughout the post-stall region investigated.

The results of the parametric investigation suggested that the effect of the control was to retain attached flow over the upper surface of the airfoil for a wider range of angles of attack. This was confirmed by the flow characterisation exercises undertaken, which demonstrated that activation of the control resulted in a massive decrease in the size of the wake region above the upper surface of the airfoil for high angles of attack.

The reattachment of the flow was attributed to the generation of a train of spanwise, negatively rotating vortices. These vortices appear to roll down the upper surface of the airfoil. Only negatively rotating vortices were observed, which suggests that the other half of the vortex pair generated by the planar ZNMF jet had been destructively interfered with by the natural instabilities in the shear layer. The coalescence of a number of smaller vortices to form a larger, more intense vortex was observed as the vortex progressed over the suction surface.

When forced at the upper optimal frequency, $F^+ = 1.3$, the spanwise vortex generated required slightly less that two entire excitation periods to convect from the leading to the trailing edge. As a consequence, at any instant in time two vortices were present over the upper surface of the airfoil. On the other hand, at the lower optimal frequency of $F^+ = 0.7$, the vortex required approximately one excitation period to convect over the same distance.

From the PLIF visualisations it was inferred that the structures generated by the ZNMF jet had been amplified by the shear layer flow such that they were at least two orders of magnitude greater than the characteristic dimension of the ZNMF jet orifice.

The extent of the vorticity inherent in the flow field was greatly reduced by activation of the control, however the maximum vorticity intensity remained relatively unchanged.

Three mechanisms through which the generated vortices affected reattachment of the flow field were proposed. Firstly, it was suggested that whilst the vortex was located close to the uncontrolled shear layer separation point, significant enhancement of the entrainment of the shear layer occurred. At this point it was also postulated that the negatively rotating vortex transferred rotational momentum to the shear layer via viscous forces. Both of these mechanisms acted to deflect the shear layer towards the airfoil surface. The final mechanism identified assisted the reattached shear layer to remain attached for phase angles for which the large-scale structure had convected further downstream. The presence of the vortex deflected streamlines away from the surface, resulting in the alleviation of the local upstream pressure gradient, thereby reducing the forces promoting boundary layer separation.

11.0 ACKNOWLEDGEMENTS

12.0 REFERENCES

Bar-Sever, A. (1988) Separation Control on an Airfoil by Periodic Forcing. *AIAA Journal*, Vol. 27, No. 6, pp. 820-821.

Cater, J., and Soria, J. (2002) The evolution of round zero-net-mass-flux jets, *Journal of Fluid Mechanics*, Vol. 472, pp. 167-200.

Chang, R., Hsiao, F. and Shyu, R. (1992) Forcing Level Effects of Internal Acoustic Excitation on the Improvement of Airfoil Performance, *Journal of Aircraft*, Vol. 29, No. 5, pp. 823-829.

Donovan, J., Kral, L. and Cary, A. (1998) *Active Flow Control Applied to an Airfoil*, AIAA Paper 98-0210.

Houghton, E. and Carpenter, P. (2003) *Aerodynamics for Engineering Students*, 5th Ed, Butterworth Heinemann, Great Britain.

Katz, Y., Nishiri, B. and Wygnanski, I. (1989) The delay of turbulent boundary layer separation by oscillatory active control, *Physics of Fluids A*, Vol. 1, No. 2, pp. 179-181.

Kostas, J., Soria, J. and Chong, M.S. (2002) Particle image velocimetry measurements of a backward–facing step flow, *Experiments in Fluids*, Vol. 33, pp. 838-853.

Lee, C., Ha, Q.P., Hong, G. and Mallinson, S. (2003) A piezoelectrically actuated micro synthetic jet for active flow control, *Sensors and Actuators A,* Vol. 108, pp. 168-174.

Maroto, J., de Dois, J. and de las Nieves, F. (2002) Use of a Mariotte bottle for the experimental study of the transition from laminar to turbulent flow, *American Journal of Physics*, Vol. 70, No. 7, pp. 698-701.

McCormick, B. (1995) *Aerodynamics, Aeronautics and Flight Mechanics*, 2nd Ed, John Wiley & Sons, USA.

Seifert, A., Bachar, T., Shepshelovich, M. and Wygnanski, I. (1993) Oscillatory Blowing: A Tool to delay Boundary Layer Separation, *AIAA Journal*, Vol. 31, No.11, pp. 2052-2060.

Seifert, A., Darabi, A. and Wygnanski, I. (1996) Delay of Airfoil Stall by Periodic Excitation, *Journal of Aircraft*, Vol. 33, No. 4, pp. 691-698.

Seifert, A. and Pack, L. (2002) Active Flow Separation Control on Wall Mounted Hump at High Reynolds Numbers, *AIAA Journal*, Vol. 40, No. 7, pp. 1363-1372.

Smith, B and Glezer, A, (1998) The formation and Evolution of Synthetic Jets, *Physics of Fluids*, Vol. 10, No. 9, pp. 2281-2297.

Smith, D., Amitay, M., Kibens, V., Parekh, D. and Glezer, A. (1998*) Modification of Lifting Body Aerodynamics Using Synthetic Jet Actuators*, AIAA Paper 98-0209, Georgia, USA.

Soria, J. (1996) An investigation of the near wake of a circular cylinder using a video-based digital cross-correlation particle image velocimetry technique, *Experimental Thermal Fluid Science*, Vol. 12, pp. 221-233.

Tomar, S., Arnaud. J. and Soria, J. (2004) Structure of a Zero-net-mass-flux round jet in crossflow, *Proceedings of the 2004 Australasian Fluid Mechanics Conference*, Sydney, Australia.

Wu, J., Lu, X., Denny, A., Fan, M. and Wu, J. (1998) Post-stall flow control on an airfoil by local unsteady forcing, *Journal of Fluid Mechanics*, Vol. 371, pp. 21-58.

Zaman, K., Bar-Sever, A. and Mangalam, S. (1987) Effect of acoustic excitation on the flow over a low Re airfoil, *Journal of Fluid Mechanics*, Vol. 182, pp.127-148.

Zaman, K. (1992) Effect of Acoustic Excitation on Stalled Flows over an Airfoil, *AIAA Journal*, Vol. 30, No. 6, pp. 1492-1499.